ORIGINAL RESEARCH ARTICLE

The Depositional Record
Open Access
A journal of the International Association of Sedimentologists

IAS WILEY

Characteristics and controls on the distribution of sublittoral microbial bioherms in Great Salt Lake, Utah: Implications for understanding microbialite development

Robert L. Baskin[1] | Giovanna Della Porta[2] (ID) | V. Paul Wright[3] (ID)

[1]RLB Research Alliance, North Salt Lake, UT, USA

[2]Earth Sciences Department, University of Milan, Milan, Italy

[3]Natural Sciences, National Museum of Wales, Cardiff, UK

Correspondence
V. Paul Wright, Natural Sciences, National Museum of Wales, Cardiff CF10 3NP, UK.
Email: v.vpw@btopenworld.com

Abstract

Side-scan sonar and Compressed High Intensity Radar Pulse mapping of Great Salt Lake, Utah, linked to reprocessing of acoustic data from bathymetric surveys, has enabled the distribution of microbial bioherms to be assessed. Bioherms occupy an estimated area >700 km^2 in the south arm and >300 km^2 in the north arm. Distributions vary from statistically dispersed to clustered, and in this latter case, are predominantly located on metre-scale, fault-controlled topographic highs, with sediment infilling intervening lows between adjacent offsets. Individual bioherms are circular to oblate and range from centimetres to over 2 m in diameter. In some areas, bioherm heights were measured at more than 1.5 m above adjacent substrate. Sublittoral bioherms are made of aragonite, calcite and minor dolomite precipitated due to physico-chemical, biologically induced and influenced carbonate mineralization processes in association with microbial mats. Bioherm fabrics vary at the millimetre to centimetre-scale and consist of leiolitic and clotted peloidal micrite-grade carbonate, sinuous threads of spherulitic fibrous aragonite crystals, laminated micrite boundstone and internal carbonate mud sediment with peloids and ooids. The identification of factors that influence microbial bioherm occurrence and spatial distribution in Great Salt Lake is limited to a set of collinear physical, chemical and biological variables that are confined to a localised closed system, such as salinity, water depth, wave energy, stable substrate and sediment accumulation. Anthropogenic modifications to Great Salt Lake resulting in increased salinity have exceeded the salinity range in which bioherm-mediating microbial communities can survive, effectively defining an upper limit of salinity for bioherm microbial community viability. The better understanding of the distribution of microbial bioherms has significant implications for managing and protecting the lake ecosystem and may provide insights into the physical and chemical controls that existed during the formation of fossil microbialites in deep time.

KEYWORDS

endorheic hypersaline lake, environmental management, Great Salt Lake, microbialites, rift basin

1 | INTRODUCTION

Great Salt Lake (GSL) in Utah hosts one of the largest populations of actively forming microbial bioherms in the world. Their existence has been known for over 80 years since Eardley's (1938) pioneering studies of sediment distribution identified the occurrence of microbial bioherms along the shallow margins of the lake. Several recent studies (Bouton et al., 2016a, 2016b; Bouton et al., 2020; Chidsey et al., 2015; Della Porta, 2015; Vanden Berg, 2019; Vennin et al., 2019) have focused on easily accessible bioherms exposed in the littoral zone and from shallow sublittoral areas. This study focuses on the sublittoral areas of the lake, where logistical problems including the low visibility due to water clarity issues, and high salinity causing difficulties of sampling and access, have prevented detailed studies. Besides documenting the restriction of actively forming sublittoral bioherms to the south arm of the lake, this study has confirmed the impact anthropogenic factors have in affecting microbialite distributions, and also the role of metre-scale fault displacements on the occurrence and distribution of the bioherms. The evaluation of microbial bioherm spatial distribution and controls is integrated with detailed investigation of the sublittoral carbonate facies at the meso and micro-scale and their geochemical stable isotope signatures.

A better understanding of the distribution of and controls on the bioherms has implications for interpreting microbialites in deep time, but also for the future management of this fragile ecosystem in which the microbial bioherms are a critical element.

2 | GEOLOGICAL AND ENVIRONMENTAL SETTING

The GSL in Utah is an endorheic, meromictic, wind-driven (in the sense of Nutz et al., 2018), hypersaline water body located in northern Utah, and is comprised of two large basins separated by a fault-controlled shoal that extends from Hat Island in the south-west to Promontory Point (Baskin, 2005, 2006; Spencer et al., 1984) (Figures 1A and 2). The GSL is the last vestige of Pleistocene freshwater Lake Bonneville, which covered over ca 51,200 km^2 at its highest level (Eardley et al., 1957; Gilbert, 1890; Madsen et al., 2001). Currently (February 2021), the south arm of GSL has a water-surface elevation of ca 1,277.9 m amsl and the north arm is at ca 1,277.75 m amsl, making the lake ca 80 km long, 18–29 km wide, with a surface area of ca 2,638 km^2, a volume of ca 11.8 km^3 and an average depth of ca 4 m. The maximum depths at 1,277.9 m amsl and 1,277.75 m amsl are ca 7.8 m
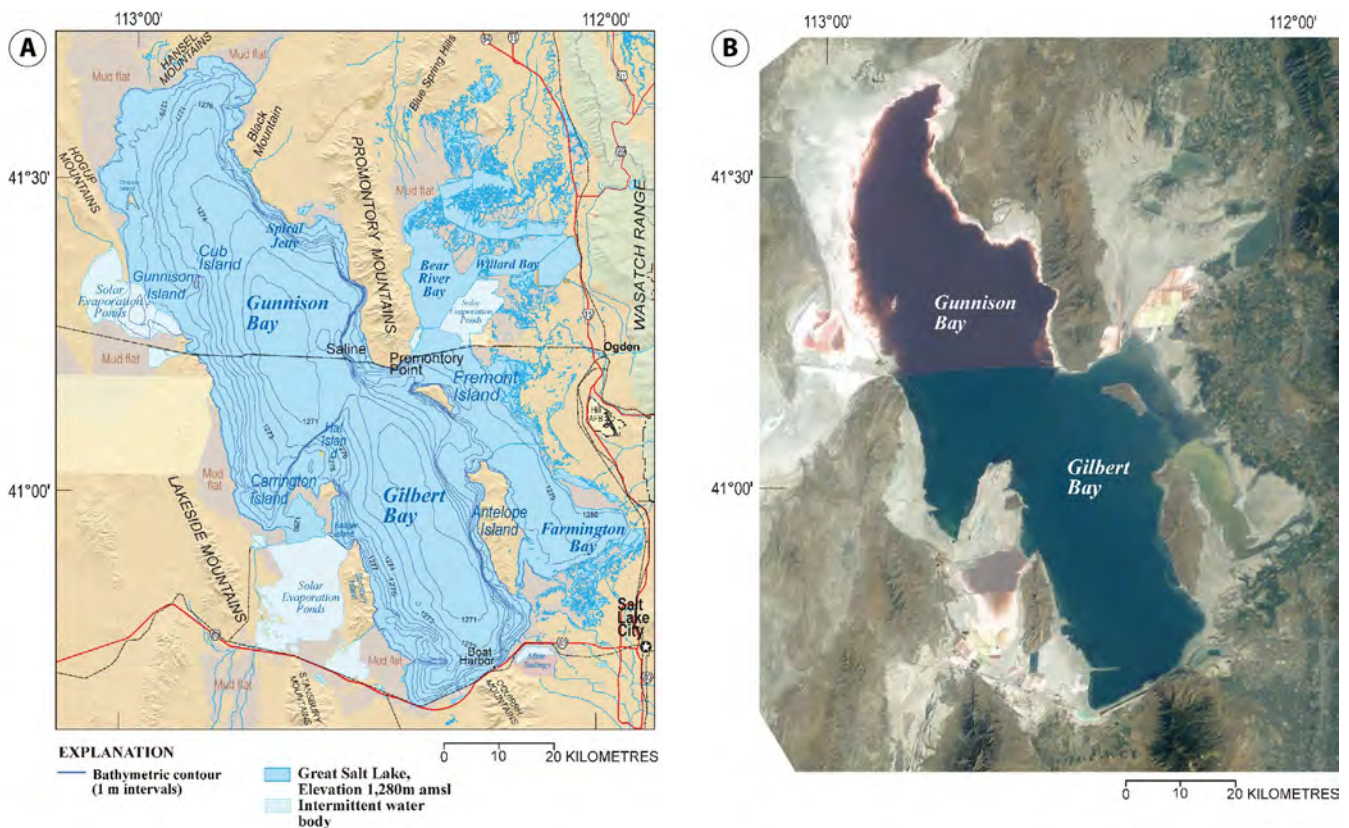

FIGURE 1 (A) Map of GSL showing bathymetric contours at 1 m interval. (B) Natural-colour satellite image of GSL. Image shows change in lake colour due to salinity-induced differences in substrate conditions and biota (halophilic microbes), north and south of the 1959 rock-filled causeway (NASA ISS07-E-13002, 19 August 2003)
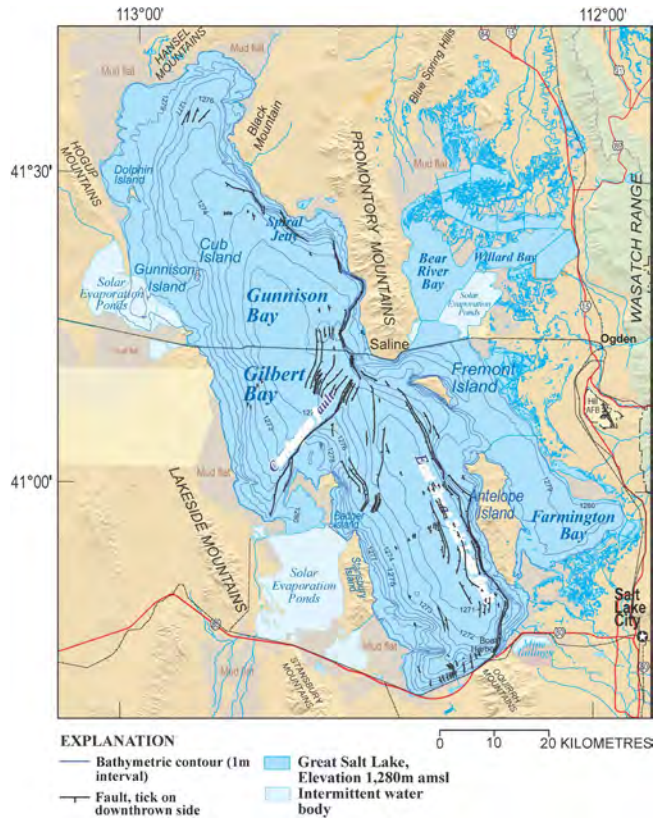
FIGURE 2 Location of known faults in GSL. East Great Salt Lake fault and Carrington fault naming conventions from Mohapatra and Johnson (1998). Colman et al. (2002) and Dinter and Pechman (2014) have referred to these same faults as the 'East Lake Fault' and 'Carrington Fault'. Fault locations adapted from Dinter and Pechmann (2014)

and *ca* 7.55 m, respectively. The lake long axis aligns along a broadly NW-SE orientation paralleling the modern prevailing wind direction. Fetch distance for prevailing winds was upwards of 121 km throughout most of GSL's existence.

The current lake occupies two Cenozoic half grabens located on the eastern edge of the Great Basin. The Great Basin is characterised by low-angle detachment faults with high-angle listric faults developed in areas above the low-angle faults (Morrison, 1966) and terminates eastward along the Wasatch fault zone, a 370 km long segmented normal-fault system. The lake is bounded to the east by the Wasatch Range (Figure 1A) and to the west by the Lakeside and Hogup Mountains (on some early maps referenced as the 'Terrace Mountains'), and the GSL Desert. To the east of GSL, in the Wasatch Range, the geology differs between three major drainages (Bear, Weber and Provo/Jordan) and the lake margins (Arnow, 1984; Bouton et al., 2020; Utah Department of Natural Resources, 1997). The eastern flank of GSL is defined by a series of north-west trending normal faults (Kowalewska & Cohen, 1998). These high angle faults conform to deep faults defined by Mikulich and Smith (1974), using data collected in 1969 (Colman et al., 2002). The East

Great Salt Lake Fault (EGSLF) lies along the west edge of Antelope Island. Where the EGSLF zone merges with the Carrington fault off Promontory Point, an overall graben-like structure is present, involving displacement of the upper-most sediments (Colman et al., 2002). The Carrington fault (Figure 2) separates the lake into two basins and trends to the north-east from Carrington Island toward the south-western tip of Promontory Point (Baskin, 2005; Colman et al., 2002; Morrison, 1966; Spencer et al., 1984). These two natural basins probably influenced circulation and sediment depositional patterns throughout much of the lake history. During periods of low lake-level elevation, the south basin of the lake would segment into two water bodies separated along the shoal formed by the Carrington fault. These natural basins differ from the Gunnison Bay and Gilbert Bay designations, which are based on the segmentation of the lake by a rock-filled railroad causeway constructed in 1957–1959, between the southern edge of Promontory Point at Saline with Lakeside to the west, replacing a wooden-trestle bridge completed in 1904. The rock-filled causeway subdivided GSL into two parts, one hydrologically connected to the south arm of the lake (Gilbert Bay/south arm) and the other a separate, isolated, inflow-limited system (Gunnison Bay/north arm) (Figure 1).

Displacement along the fault segments underlying the eastern margins of the lake differed for most of the late Neogene (Kowalewska & Cohen, 1998), resulting in differences in sedimentation rates and varying environmental conditions between the north and south basins throughout much of the late Pleistocene (Moutoux, 1995). Subsidence rates were highest along the eastern margins of the basins, close to the faults, and subsequently had the highest sedimentation rates. Dating suggests average long-term (5 Myr) exhumation rates of 0.2–0.4 mm/year for most of the Wasatch Range (Armstrong et al., 2004).

Correlation of recent seismic profiles with sediment cores indicates that the oldest post-Lake Bonneville sediments (*ca* 13.5 ka) have been displaced multiple times since their deposition, including at least three episodes of movement on the EGSLF totalling as much as 12 m (Colman et al., 2002). Topographic expressions of fault displacement on the lake floor, as reported by Colman et al. (2002) and Dinter and Pechmann (1999), and imaged during this study, are strong evidence that the area remains tectonically active (Baskin, 2005, 2014; Kowalewska & Cohen, 1998).

Underlying GSL are Neogene deposits (Kowaleska & Cohen, 1998) representing marsh and shallow lacustrine conditions, that began accumulating in the north basin nearly 5 Ma (late Miocene–Early Pliocene), with a major expansion of open water environments only in the Middle Pleistocene. Lacustrine environments reached their maximum aerial extent at about 0.6 Ma. Large but frequently saline lakes occupied the north basin after about 0.6 Ma. In the south basin,

ephemeral, saline lacustrine conditions started at 2.1 Ma and developed to full lacustrine conditions at 0.3 Ma (Kowalewska & Cohen, 1998).

Lake Bonneville was a hydrographically closed basin during its transgressive phase from *ca* 28 ka to *ca* 15 ka. At its highest level, it breached Red Rock Pass in Idaho, flowed into the Snake River drainage and catastrophically dropped, losing nearly 100 m of elevation (Gilbert, 1890; Jones et al., 2009; Malde, 1968; O'Connor, 1993; Oviatt, 2015) and leaving behind the Bonneville-level shoreline (Jones et al., 2009; Figure 3). The lake continued to discharge into the Snake River Basin for nearly 2,500 years, during which time the Provo-level shoreline formed around the basin (Figure 3). From the Provo shoreline, a rapid regressive phase started at *ca* 12 ka and dropped the lake level to elevations comparable to modern GSL (about 11 ka). Around 10 ka a brief transgression produced the Gilbert shoreline and then lake level dropped again close to its present-day level (Jones et al., 2009).

2.1 | Climate, hydrology and water chemistry

The climate of GSL and vicinity is semi-arid with average annual temperatures ranging from 4.6 to 17.6°C at the Salt Lake City International Airport. Annual mean water temperature in the south arm of GSL for 1994–2006 was greatest in July–August (25.9°C) and lowest in January–February (1.6°C) (Belovsky et al., 2011). Average annual precipitation ranges from less than 250 to 410 mm on the valley floors to greater than 1,770 mm in the high mountain areas. The vast majority (*ca* 95%) of freshwater entering GSL originates in the Wasatch Range as spring snowmelt runoff and discharges to the south arm of the lake.

The GSL drainage basin is approximately 55,684 km^2 with annual inflow to the lake being *ca* 3,577,118,100 m^3; inflow and evaporation vary based on climate conditions (Waddell & Barton, 1978). The GSL has a much greater surface-area-to-volume ratio than other lakes in the region, and as a result, an average of about 3,580 hm^3 evaporates from the lake each day (Waddell & Barton, 1978). Groundwater discharge into GSL is difficult to quantify as the extent of the lake, lake levels, water quality and density, and baseflow from rivers fluctuate over time and affect the rate and locations of groundwater flow to the lake. Most measured groundwater discharge to GSL is from springs located onshore or nearshore and was estimated during a relatively dry 1961/1962 period, at about 4% of the total (Arnow & Stephens, 1990; Hahl & Langford, 1964; Loving et al., 2000; Waddell & Barton, 1978; Waddell & Bolke, 1973; Waddell & Fields, 1977; Wold et al., 1997). In modern time, GSL has experienced marked fluctuations in lake level (Figure 3). For example, in 1963, GSL was at its lowest water-surface elevation in recent history being *ca* 1,277 m amsl and covering an expanse of about 2,460 km^2. At its highest water-surface elevation in 1986, the lake surface was at *ca* 1,284 m amsl and covered an area just over 6,216 km^2.

Historical salinity in GSL varies from as high as 27% in the north arm, to 12%–27% in the south arm. Lake water pH is *ca* 7.9–7.6 up to 8.4 at Bridger Bay; alkalinity has values of 8.4 mEq/L at Bridger Bay and 5.4 mEq/L at Promontory Point; lake water Mg/Ca varies from 9 to 115 (Della Porta, 2015; Diaz et al., 2009; Jones et al., 2009; Kowalewska & Cohen, 1998; Pedone & Folk, 1996; Reitner et al., 1997). The GSL is supersaturated with respect to calcium carbonate
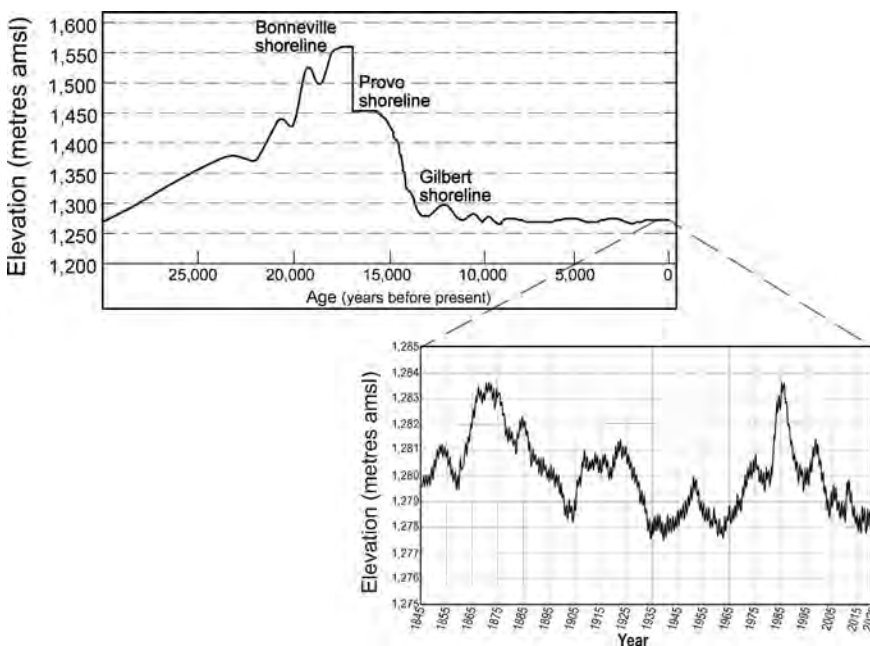

FIGURE 3 Generalised hydrograph of Lake Bonneville and historical record of lake levels in the south arm of GSL (Lake Bonneville hydrograph adapted from Murchison, 1989; Oviatt, 1997, 2015; Oviatt et al., 2015). The GSL historical data from: Pre-1843 (Gilbert, 1890), Fremont, 1843 (Miller, 1980); 1847–1874 (Gilbert, 1890); 1875–1938, various organisations (Arnow & Stephens, 1990; Gilbert, 1890); 1939–Present, U.S. Geological Survey records

throughout the year and supersaturation increases during the summer months (Corsetti et al., 2013). Recently, Bouton et al. (2020) evaluated the calcium ion budget and dynamics at the basin scale, from the source from erosion of substrate rocks to transport and sink in the lake water column and sediment determining a mass balance for the Holocene GSL.

Segmentation of the lake by the construction of the causeway since 1959 has effectively limited the supply of fresh water and sediment to the north arm and has affected water chemistry, wave-base conditions, circulation patterns and the biological communities (Figure 1B). Currently (February 2021), the difference in water-surface elevation is *ca* 0.15 m. Evaporation exceeds inflow in the north arm and results in a net northward flow of water and its dissolved constituents from the south arm to the north. Under suitable conditions, density-driven currents form and bi-directional flow occurs through the causeway. Less dense water from the south flows to the north and higher density water from the north flows to the south. As the higher density water from the north arm enters the south arm, it sinks beneath the less dense south arm water and forms a persistent chemocline-delimited stratification layer between 5 and 7 m beneath the surface. A deep anoxic layer of hypersaline water (*ca* 25% salinity) is overlain by an oxic upper layer (*ca* 15% salinity). Mixing between the layers is through diffusion, circulation and internal waves (Jones & Wurtsbaugh, 2014; Spall, 2008).

Topographical, bathymetric and atmospheric conditions control circulation patterns in the lake. Circulation in the south arm of GSL is counterclockwise (Hahl & Handy, 1969; Katzenburger & Whelan, 1975; Lin, 1976; Rich, 2002; Spall, 2008). Evidence of historical effects of currents are found in numerous, commonly ooidal bars and spits (Spall, 2008). A very large (>100 km^2) relict beach ridge system is present north of Rozel Point.

2.2 | Lake biota

The GSL biota composition is affected by salinity fluctuations. The organisms identified are: brine flies *(Ephydra cinerea, E. hians)*, brine shrimps *(Artemia franciscana),* green algae *(Dunaliella viridis, D. salina)*, protozoa and halophilic microbes (Post, 1977; Stephens, 1974, 1990, 1998). Various other studies also identified diatoms, ostracods, gastropods and fungi (Baxter, 2018; Eardley, 1938; Kjeldsen et al., 2007; Reitner et al., 1997). The compilation edited by Baxter and Butler (2020) provides a detailed review on the biology of GSL. Phytoplankton have been documented by Belovsky et al. (2011). Benthic microbial mat compositions were investigated by several authors reporting the presence of halophilic archaea, heterotrophic bacteria including sulphate-reducing bacteria, cyanobacteria and viruses (Almeida-Dalmet et al., 2015, 2018; Baxter, 2018; Kjeldsen et al., 2007; Lindsay

et al., 2017; Reitner et al., 1997; Wurtsbaugh et al., 2011 and references therein). Lindsay et al. (2017, 2019) reported the results of SSU rRNA gene analyses reporting differences in the microbial communities in the south and north arms. The former is more productive, has more abundant photoautotrophs (cyanobacteria, diatoms and green algae), and has actively forming microbialite interpreted as linked to the cyanobacterium *Euhalothece* and the diatom *Navicula* (Lindsay et al., 2017).

2.3 | Lake sediments

The earliest published work on GSL sediment distribution and its bioherms is by Eardley (1938), who provided a map from 1933 including 'calcareous algal bioherms, oolites, lake clays and valley alluvium, and bedrock—generally mountainous areas'. Detrital grains consist of quartz, hornblende, orthoclase, albite, whereas clays are dominant on the lake bottom from a depth of 4 m (Eardley, 1938). Other minerals identified in GSL are: (a) kaolinite $Al_2Si_2O_5(OH)_4$ forming also concentric bands within the ooids, (b) illite, montmorillonite and probably sepiolite $Mg_4Si_6O_{15}(OH)^2 \cdot_6(H2O)$, which have been suggested to be present as detrital material but also to form within the lake sediment (Eardley, 1938), (c) pyrite and (d) hydrous Mg silicate (Eardley, 1938; Grim et al., 1960).

According to Eardley (1938), precipitated carbonates have an average of 66.4% aragonite, 11.8% dolomite, 2% organic matter, 20% insoluble material, and compare with recent studies (Pace et al., 2016; Pedone & Folk, 1996). Fabric-preserving Ca-rich dolomite, as cement and replacement of aragonite, has been described from a tufa mound on the west lake side by Pedone and Dickson (2000). Bouton et al. (2016a) and Pace et al. (2016) reported that on the exposed bioherms, dolomite is present in the pore space, and that in the submerged bioherms, Mg clays form through microbially mediated and early diagenetic processes, and aragonite is partially dissolved and replaced by dolomite (Pace et al., 2016). Dunham et al. (2020) identified proto-dolomite from shoreline cores, suggesting that it is abundant in sediment cores from the south arm and is rare in cores from the north arm.

Observations by Eardley in 1934 (Rawley, 1974) indicate that the entire bottom of the lake was crusted over with halite crystals. Where sampled, the salt thickness ranged from *ca* 25 mm to *ca* 150 mm. However, halite was not observed in the south arm of the lake in 1933 and in the north arm of the lake in 1932. Low lake levels between 1934 and 1940 probably maintained a variably thick salt crust over much of the lake floor; rising lake levels between 1945 and 1955 probably dissolved the salt crust. Precipitation of salt in the north arm probably began between 1959 and 1960, shortly after the

completion of the rock-filled causeway. Although additional observations of salt deposition in the south arm were made during the record low lake levels of 1959–1963 (Hedberg & Parry, 1971), these deposits were short-lived and subsequently dissolved as freshwater inflows lowered the salinity of Gilbert Bay. In the north arm, mud flats are characterised by evaporite mineral precipitation, mostly halite but also gypsum. Mirabilite precipitates in suspension ($Na_2SO_4 \cdot 10H_2O$) in lake water (Eardley, 1938).

The GSL has gently sloping, ramp-like shorelines (Baskin, 2005, 2006; Carozzi, 1962; Eardley, 1938), forming mud or sand flat shorelines, and as a result lake level fluctuations produce wide shifts of the shoreline. High-energy shorelines (especially the eastern side exposed to the north-westerly winds) are characterised by ooidal sand and bioherms (Carozzi, 1962; Eardley, 1938; Halley, 1976). The GSL aragonitic ooids have been the focus of several studies (Halley, 1977; Kahle, 1974; Pedone & Norgauer, 2002; Reitner et al., 1997; Sandberg, 1975; Trower et al., 2020).

Following Eardley (1938) mapping, microbial bioherms were investigated by Carozzi (1962). Halley (1976) reported an extent of only 100 km^2 for microbial bioherms (vs. Eardley's, 1938 estimate of 100 mi^2—259 km^2). Spencer et al. (1984) identified 'biohermal mounds and ridges' in the vicinity of Carrington Island and carbonate pavements between Carrington Island and Promontory Point. These 'biohermal mounds and ridges' correspond with Eardley's areas of calcareous algal bioherms for the Carrington Island area; however, the carbonate pavements mentioned by Spencer et al. (1984) are not included in Eardley's original map. In the limited published acoustic data, Spencer et al. (1984) observed that 'many bioherm mounds coincide with fault traces. The mounds also seem to be rooted in a reflector located approximately 2 m below bottom …' in areas where the 'reflector indicates a buried strand line at about 1,275 m'. Colman et al. (2002) discussed the presence of possible bioherm structures above some faults and the fault-controlled ridge connecting Carrington Island and Promontory Point. In many cases, the mounds appeared rooted in the Holocene sediments, and were commonly associated with faults. Colman et al. (2002) interpreted these mounds to be bioherms, similar to those around the shore of the lake, and suggested that those located above faults may have formed by enhanced carbonate precipitation where basinal fluids migrated up along fault traces.

Della Porta (2015), Chidsey et al. (2015), Pace et al. (2016), Bouton et al. (2016a), Vennin et al. (2019) and Vanden Berg (2019) described a range of microbial macro to micro-scale features including forms on gravity flow deposits (Bouton et al., 2016b). Bouton et al. (2016a) reported a non-random distribution of microbial bioherms with polygonal organisation and fault parallel alignments; in particular, aligned microbial bioherms may underlie normal

faults parallel to the Wasatch Range, as similarly suggested by Colman et al. (2002). Bouton et al. (2016a) distinguished different types of bioherms based on morphology from exposed shoreline to offshore: fossil cauliflower and laminated structures dated to *ca* 21.9 ka; decimetre to metre-wide structures (from 10.6 ka to present) consisting of laminated and clotted mesofabrics and covering a large area by coalescing (thickness 2–30 cm), which correspond to Vanden Berg's (2019) ring structures; 'oncoids' with a clotted mesofabric, resulting from the erosion of microbial mats, that accumulate along the shoreline; domes and columns with diameters of 0.2–1.2 m, as noted in Della Porta (2015), with clotted and laminated mesofabrics; and pustular crust ridges corresponding to Vanden Berg's (2019) microbialite ridges. All these authors identified domal to columnar forms occurring in sublittoral near-shore areas.

Several studies have evaluated the mechanisms of carbonate precipitation of GSL bioherms related to possible microbial mediation. Eardley (1938) suggested that carbonate precipitation was controlled by the amount of HCO_3^-, CO_3^{2-}, CO_2, NaCl and Na_2SO_4 in the water, rates of evaporation, microbial photosynthesis and metabolism. Carozzi (1962) proposed that cyanobacteria photosynthetic CO_2 uptake promoted carbonate precipitation. Pedone and Folk (1996) showed that, in some cases, bacterially mediated aragonite precipitation starts from brine shrimp eggs during the degradation of their organic matter, with further growth of prismatic aragonite cement interpreted as abiotic. According to Reitner et al. (1997), carbonate precipitation was restricted to a narrow zone at the base of the microbial biofilm covering the bioherm top, made of the cyanobacteria *Gloeocapsa* and *Aphanothece packardii* associated with heterotrophic bacteria, via organomineralic processes linked to sulphate reduction. The abundance of sulphate-reducing bacteria was suggested by Kjeldsen et al. (2007) who reported that the strong emanations of H_2S from all the lake clay sediment betrays the presence of abundant sulphur bacteria. The role of microbes in the formation of bioherms was more recently reviewed by Della Porta (2015), Pace et al. (2016), Lindsay et al. (2017, 2019, 2020) and Dunham et al. (2020). Due to the lack of *Euhalothece* and *Navicula* in the north arm, Lindsay et al. (2017, 2019) concluded that the north arm microbialites are remnant, preceding the partial isolation of that area following the causeway construction and increased salinity. Conditions in the north arm, averaging about 27% salinity, appear to have exceeded the environmental range of survival for cyanobacteria and diatoms, considered responsible for carbonate precipitation forming GSL bioherms (Lindsay et al., 2017, 2019).

The stable isotope geochemical signature of GSL ooids and microbial bioherms was investigated by various authors displaying similar values (Della Porta, 2015; Newell et al., 2017; Pedone & Norgauer, 2002) and concluding that GSL carbonates precipitated in equilibrium with modern lake

water. Ingalls et al. (2020) proposed that some values might reflect local isotopic disequilibrium driven by microbial metabolism during authigenic carbonate precipitation.

3 | MATERIAL AND METHODS

3.1 | Acoustic data and bathymetric survey

To define the occurrence and spatial distribution of microbial bioherms in GSL, acoustic data from bathymetric surveys (Baskin, 2005, 2006; Figure 4A) were reprocessed to preserve original variations in depth, and to provide a lake-wide probabilistic data set that could be used for statistical examination of changes in acoustic substrate roughness. To retain original acoustic roughness characteristics of the benthos, each data point was corrected for water-column sound velocity; no smoothing or averaging was applied during reprocessing. The reprocessed data were exported to ASCII data tables and subsequently used for calculation of acoustic benthic rugosity. Geographic reference information was calculated for each transect segment by deriving an average position from each subset of data along all transects and assigned to the appropriate calculated rugosity. Retention of the geospatial component of rugosity variation allowed for examination of not only the rugosity of a surface but the change in rugosity across a surface and the spatial distribution of roughness. The methodology also reports adjacent maximum and minimum benthic altitudes and allows for calculation of statistics on the physical heights and locations of benthic formations.

A custom computer program was written to test the effects of varying transect subset length on rugosity values and derive average location, maximum and minimum benthic altitudes, and statistics on the physical heights and locations of benthic formations for each transect subset.

Rugosity is mathematically defined as:

$$R_a = \frac{1}{N} \sum_{j=1}^{N} |r_j|$$

where R_a is the calculated rugosity (m); N the number of points included in the calculation (limit of summation); j, index of summation; $|r_j|$ the absolute value of the vertical distance from the mean line that is statistically a very stable, repeatable parameter. Its primary use is in determining the roughness of
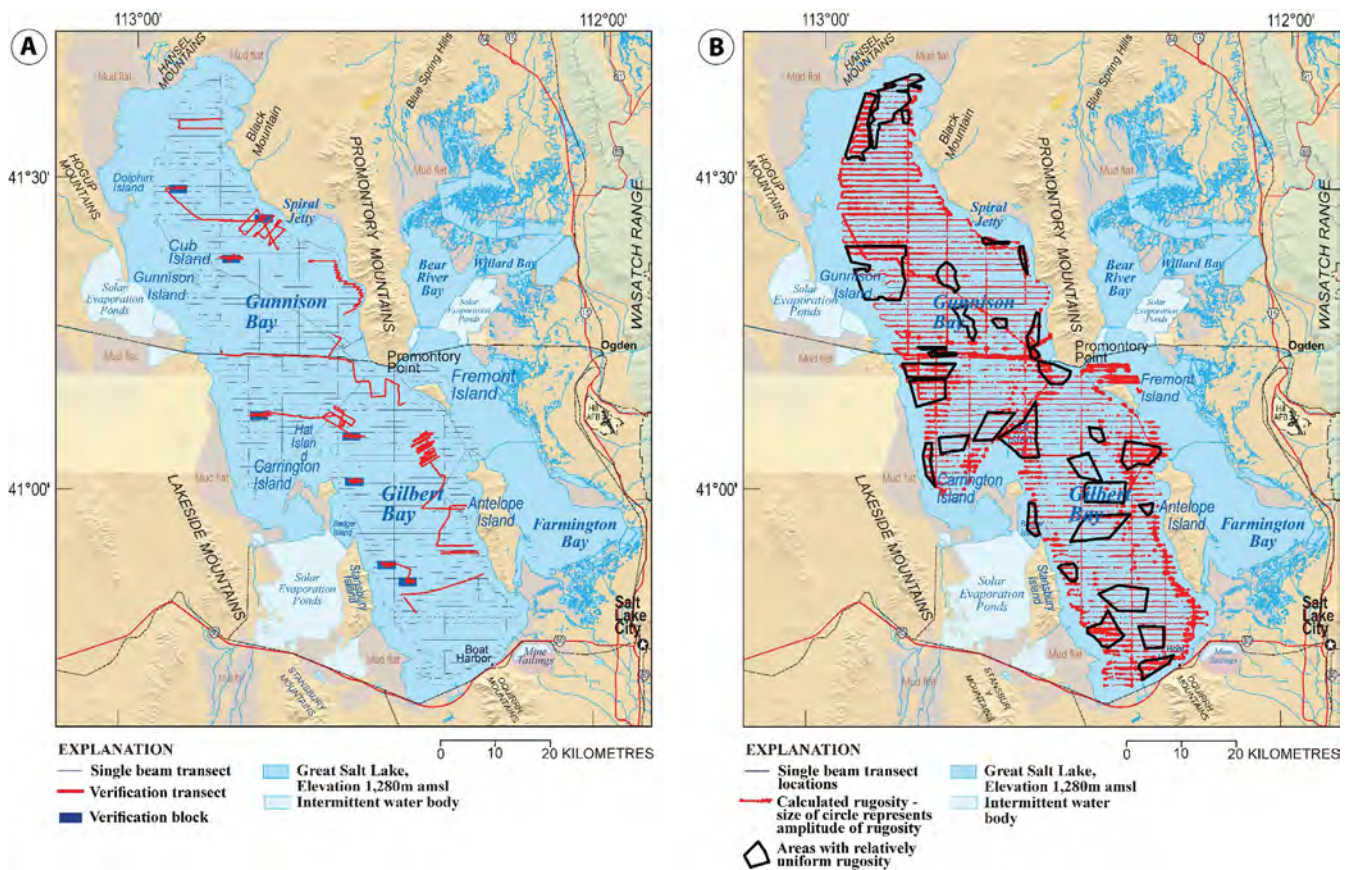

FIGURE 4 (A) Map of GSL showing side-scan sonar and CHIRP geophysical verification blocks and transects surveyed during this investigation. (B) Map of GSL showing extent of original bathymetric single-beam data and location of selected polygonal areas with relatively uniform rugosity

industrial surfaces. Nevertheless, it is also used as an important ecological parameter (Friedlander & Parrish, 1998).

Benthic rugosity was calculated for linear subsets of single-beam acoustic data along more than 1,690 km of transects for the south arm and more than 1,200 km for the north arm of the lake. Calculations of rugosity for each of the bathymetric transects used during this study were performed on 50, 100, 250 and 500-point windowed sets of data. At an average of 3–5 points per metre, this equated to approximately 10–15, 20–33, 50–63 and 100–166 m subset intervals with mean lengths of 14, 29, 72 and 143 m, respectively.

Results from the 50-sample interval subsets were imported into a Geographic Information System (GIS) along with the average position of each subset to examine the overall distribution of rugosity values and define an area of probable occurrence of microbial bioherms for use in subsequent calculations. The 50-sample rugosity calculation provided the most accurate positional information and was ultimately used in determining the transition between highly rugose and lesser rugose areas and production of a general occurrence/ non-occurrence rugosity classification map.

Rugosity values from the 50-sample data set were grouped into 10 classes based on a geometric interval and plotted on a base map of GSL using their calculated average position. Nineteen individual polygons with relatively uniform rugosity were identified for the south arm of the lake and 15 for the north (Figure 4B). Each selection was based on the uniformity of values in a 10-class geometric interval classification. Rugosity values from each 50-sample rugosity data set were grouped into 10 classes and plotted using their calculated average position. Arithmetic mean rugosity and standard deviation for each polygon were used to define high rugosity areas (as suspected bioherm occurrences) from low rugosity areas (suspected finer-grained sediments, i.e. not bioherms). Subsequent analyses of the rugosity data involved basic statistical analyses, classification of statistically 'like' subsets of roughness data, and application of spatial analysis measures of clustering.

To test for spatial patterns in the lake-wide distribution of microbial bioherms in GSL, a simple global statistical measure of clustering, Moran's *I* (Moran, 1950), was utilised. The Moran's *I* statistic utilises the value of a feature, in this case—rugosity, instead of just location to determine if there is a pattern of occurrence within the study area. It compares the values of calculated rugosity of neighbouring features to the mean value of calculated rugosity for the entire data set. A non-random spatial distribution of microbial bioherms in GSL would suggest that at least one factor, such as depth, aspect or salinity, influences bioherm distribution.

To further quantify the distribution of bioherms in GSL, a local statistical measure of clustering, 'Getis-Ord Gi*' was applied to the data (Getis & Ord, 1992). This method compares a subset of rugosity values in the data set with the rugosity values of the neighbouring features. This method provides the spatial locations of high and low rugosity value clusters. Unlike similar spatial statistics (Gi, Quadrat, Ripley's *K*) which are based solely on the spatial attributes of data, the 'Gi*' statistic allows data values (in this case, rugosity) to be included in the calculation. The Gi* statistic identified those clusters of points with rugosity values higher or lower in magnitude than expected given randomly distributed rugosity values.

3.2 | Verification of bioherm occurrence using acoustic data

Due to general low visibility throughout the water column, acoustic remote-sensing methods, direct observation (where possible), and substrate sampling were used for field-verification and determination of microbial bioherm distribution. To verify the rugosity-based determination of microbial bioherm occurrence in GSL, a series of systematic verification surveys was performed in selected areas of the lake that exhibited increased single-beam acoustic rugosity. Acoustic geophysical data from side-scan sonar and CHIRP (Compressed High Intensity Radar Pulse) systems were gathered in blocks of overlapping transects in eight areas, and in areas of widespread bioherm occurrence where time and budget constraints otherwise prevented collection of overlapping transects (Figure 4A). Data were gathered as overlapping transects to provide a larger two-dimensional distribution of benthic bioherm occurrence. The total length of transects in 'Blocks' was 147 km with a mean of *ca* 1,971 m per transect. The total for all verification lines (including blocks), was 479 km with a mean of 2,630 m per transect. All eight areas selected for verification included transitions between mapped rugose and non-rugose areas in an attempt to capture changes in substrate conditions. To remove bias that may have been introduced during the selection of verification sites, additional transects were randomly surveyed to verify the relationship between rugosity and bioherm occurrence.

3.3 | Examination of sub-bottom controls on bioherm distribution

To examine possible structural, environmental and sedimentological influences on microbial bioherm occurrence and spatial distributions, an Edgetech swept-frequency digital CHIRP (1–15 kHz) sub-bottom profiler was used along with a dual frequency side-scan sonar. To ensure comparative validity of the data, acquisition system parameters for both the side-scan sonar and CHIRP systems remained constant during the course of this investigation with both systems sharing a single 1 Hz WAAS GPS NMEA positional data string

FIGURE 5 Relationship between benthic rugosity, microbial bioherm occurrence and tectonically induced microtopographic offsets along the western margin of the main body of GSL. (A) Single-beam bathymetry showing variations in rugosity and depth associated with microbial bioherm occurrence. (B) Calculated rugosity along bathymetric transect. (C) Side-scan mosaic across a subset of varying rugose/non-rugose data showing three microbial bioherm deposits (lighter areas) and intervening lows (darker areas). The intervening lows are infilled with onlapping sediment and exhibit less backscatter. Image date 11 July 2009
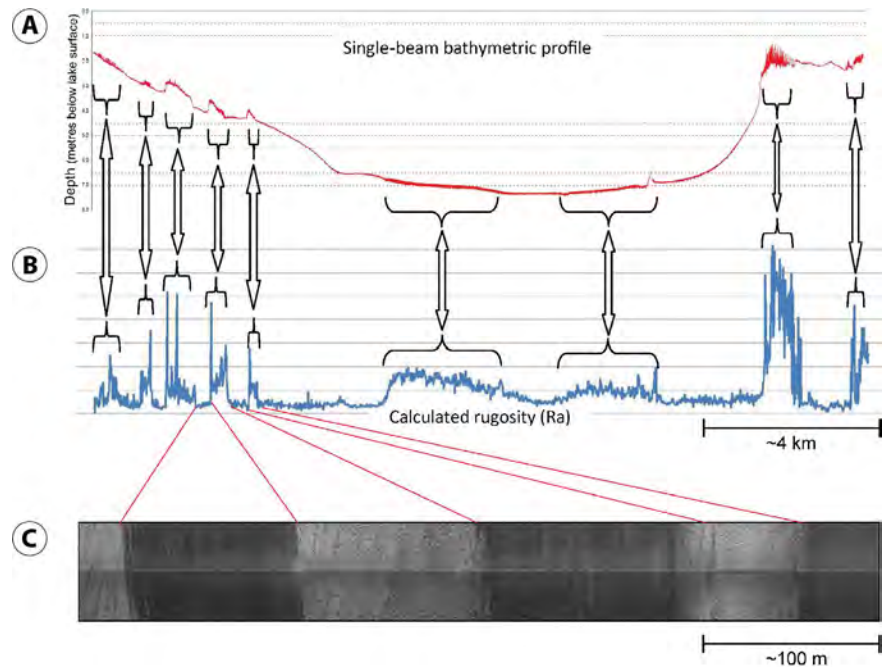
to ensure positionally co-registered data sets. The CHIRP geophysical data were used in this effort to: (a) examine the types, patterns and degrees of structural deformation beneath areas of microbial bioherm occurrence; (b) determine the general acoustic characteristics of sediments beneath and adjacent to bioherms; (c) identify acoustic signatures that could indicate possible buried bioherms; and (d) provide information that could be used to examine structural influences on bioherm occurrence. Identification of basic structural features included faults, folds, monoclines, horsts, grabens and other evidence of tectonic deformation. Depositional features included varying thicknesses of acoustically similar sediments and distinct sedimentary build-ups.

3.4 | Microbial bioherm and surrounding sediment sampling and analyses

Microbial bioherm samples were collected by professional divers in sublittoral locations 3.5–4 km away from the shoreline at water depths of approximately 3–4 m during two boat cruises (run by Cross Marine Projects Company) in July 2011 and September 2012. The lake bottom of these specific sites was imaged with side-scan sonar and videos were filmed during the dives and sampling. The three offshore sublittoral sampling locations are as follows: nearly 3.5 m NW of Bridger Bay (Lat N 41°04′01.1″, Long W 112°17′11.54″; Lat 41°03′39.23″, Long W 112°17′56.41″), east of the footwall of the East Great Salt Lake fault (EGSLF), and *ca* 4 km south of Promontory Point (Lat 41°10′58.22″, Long W 112°28′22.44″), as well in a footwall location with respect to the EGSLF (Figure 2, Figure S1). For comparative purposes microbial bioherms and surrounding sediment samples were

also collected along the shorelines at Bridger Bay (Antelope Island) and in several locations when they were exposed during times of low lake level in the months of September and October 2010. Water temperature, pH and electrical conductivity were measured directly in the field with a handheld Mettler Toledo SevenGo Duo pro™ pH/ORP/Ion/Conductivity meter SG78.

Collected samples were examined through petrographic analysis of 29 thin sections with a polarized light microscope. Cathodoluminescence (Supporting Information) was performed on 12 thin sections with a luminoscope CITL Cambridge Image Technology Limited, Cambridge, UK (model MK 5-2 operating system at 10–14 kV with a beam current between 300 and 600 µA, and vacuum gauge 50–70 millitor) at the Earth Sciences Department, University of Milan, Italy.

Scanning electron microscope (SEM) analyses were performed on 26 polished slabs and freshly broken surfaces, gold coated, with a Cambridge Stereoscan 360, operating at 20 kV with working distance of 15 mm at the Earth Sciences Department, University of Milan. Mineralogy of five carbonate powder samples (Supporting Information) was determined with an X-ray Powder Diffractometer Philips X'Pert MPD with a high temperature chamber at the Earth Sciences Department, University of Milan.

Stable oxygen and carbon isotope samples were microdrilled to separate different fabric types. Twenty-five O and C isotope analyses (Supporting Information) were performed using a MAT253 mass spectrometer with automated carbonate preparation device (Gas bench II) at the Institute for Geology, Mineralogy and Geophysics stable isotope facility, University of Bochum, Germany. Stable isotope results were calibrated to the VPDB scale by the international standards
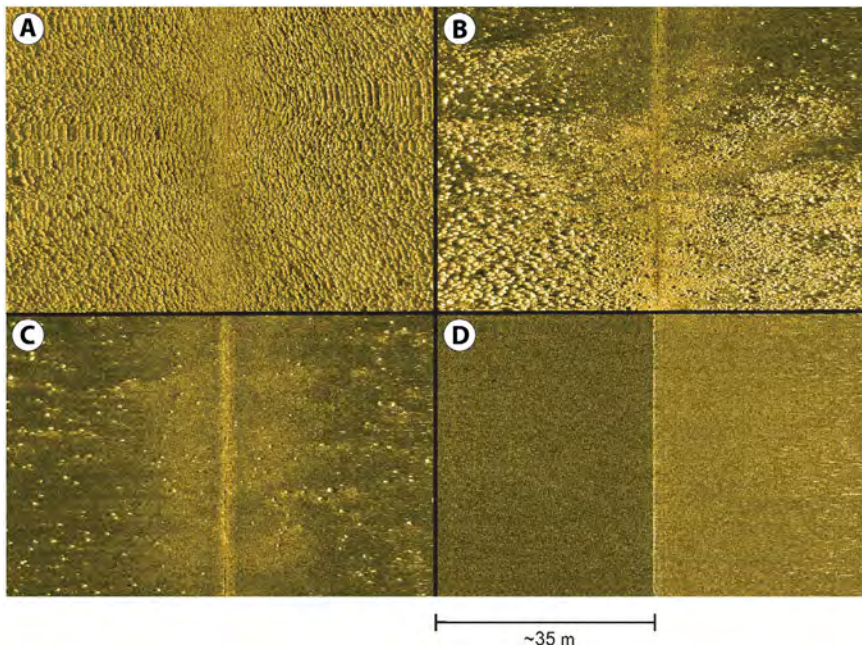
FIGURE 6 Side-scan sonar images of GSL. (A) Statistically clustered microbial bioherm deposits. (B) Transitional area from clustered bioherms to a dispersed bioherm distribution. (C) Dispersed bioherm distribution. (D) An area characterised by mud and fine sands in the south arm of GSL

CO-1 and CO-8. The analytical precision was better than 0.07‰ for $\delta^{13}C$ and 0.13‰ for $\delta^{18}O$.

4 | RESULTS

4.1 | Lake bottom survey and microbial bioherm spatial distribution

Lake-wide calculations of rugosity for the 50-sample data set from the south arm of GSL had an average value of 0.021 with a variance of 0.0016. In the north arm of the lake, the 50-sample data set had an average calculated rugosity value of 0.014 with a variance of 0.0005. Calculated rugosity abruptly increased in areas where analogue data from the bathymetric surveys showed high-frequency, high-amplitude changes occurred at the sediment–water interface (Figure 5). For the 34 polygon subsets with relatively uniform rugosity values (Figure 4B), mean rugosity was higher than the median for all 19 data sets in the south arm of the lake, indicating a positive skewness. The average of the statistical means and standard deviations for the subsets with the six largest variance values resulted in a mean rugosity value of 0.04734 and mean standard deviation value of 0.044. The average of the statistical means and standard deviations for the subsets with the six lowest variance values resulted in a mean rugosity value of 0.0061 and mean standard deviation value of 0.0027. Values greater than the mean high rugosity of 0.047 were used as a surrogate for microbial bioherm occurrence in the south arm of GSL. For the north arm of the lake, mean rugosity was higher than the median for 12 of the 15 polygon-based data sets, indicating a predominately but not uniform positive skewness. The average of the statistical means and

standard deviations for the subsets with the five highest variance values resulted in a mean rugosity value of 0.071 and mean standard deviation value of 0.062. The average of the statistical means and standard deviations for the subsets with the six lowest variance values resulted in a mean rugosity value of 0.0063 and mean standard deviation value of 0.0027. Values greater than the mean high rugosity of 0.071 were used as a surrogate for microbial bioherm occurrence in the north arm of GSL.

Results from the Moran's I analysis on the lake-wide data set showed statistically significant clustering of rugosity within the analysed 50-sample, 250-sample and 500-sample data sets. Moran's I values for the south arm of the lake were 0.54, 0.29 and 0.47, respectively, with positive Z-scores of 517, 15 and 74: Z-scores that show there is less than a 1% probability that the observed spatial distribution of substrate rugosity in the south arm of the lake could be the result of random chance. Moran's I values for the north arm of the lake were 0.34, 0.34 and 0.49, respectively, with positive Z-scores of 729, 146 and 101: Z-scores that show there is less than a 1% probability that the observed spatial distribution of substrate rugosity in the north arm of the lake could be the result of random chance.

Results from the local Getis-Ord Gi* analysis on the lake-wide data set showed statistically significant clustering of large rugosity values along the margins of the lake, similar to the results of the Global Moran's I statistic. The analysis of the 50-sample rugosity data set for a local Getis-Ord Gi* statistic exceeded the capability of the computer used during this investigation. However, the analysis of both the 250 and 500-sample interval data sets using the local Getis-Ord Gi* statistic resulted in Z-score values that indicate, at a 95% or greater confidence level, that there is a statistically significant

degree of clustering in the calculated rugosity values. The results of the local Getis-Ord Gi* analysis support the findings from the Moran's *I* statistic: there is less than a 1% probability that the observed spatial distribution of substrate rugosity could be the result of random chance.

Side-scan sonar data, visual observations and substrate samples verified that microbial bioherms were directly associated with increased calculated rugosity in all eight verification blocks and along randomly surveyed transects (Figure 4B). In areas of mapped lower rugosity, microbial bioherms were absent or widely dispersed enough to not affect the overall calculated rugosity results. Microbial bioherms in GSL vary from dispersed to laterally connected coalesced forms throughout shallower areas of the lake above an elevation of *ca* 1,273.7 m amsl (Figure 6). Areas lacking microbial bioherms were primarily located below that level, locally along the margins of the lake, or limitations in the 50-sample calculated method effectively masks their occurrence. The GSL water level is dynamic, and in historic times has varied by as much as 6 m (Figure 3). Transitions between non-bioherm areas to areas where bioherms occur range from gradual, occurring over horizontal distances ranging from tens of metres to over a kilometre, and within 1 m to a few metres vertically, to abrupt, especially across faults. Individual bioherms range in size from centimetres to over 2 m in diameter and bioherm heights have been measured at more than 1.5 m above surrounding substrates.

Microbial bioherms, ranging from individual forms to extensive coalesced assemblages, occupy an area of about 700 km^2 in the south arm, with bioherm occurrence along the shallow margins of the north arm greater than 300 km^2 (Figures 7–9). The estimate of microbial bioherm extent in the north arm of the lake is limited to areas where there is no salt cover on the lake floor (Figure 8). Thick salt deposits in the deeper areas and acoustically defined rugosity in sub-bottom geophysical data suggest that widespread occurrences of microbial bioherms existed in the north arm of GSL before the onset of extensive salt deposition.

In the verification survey areas of the south arm of the lake, faults and folds are apparent in the CHIRP profiles and coincide with microtopographic offsets and abrupt edges of linear coalesced assemblages of bioherms (Figure 10). At the base of the footwall ramp, bioherm distributions generally grade into finer-grained sediment and, in some cases, appear to be completely buried by onlapping sediment. Stratigraphic horizons directly underlying the microbial bioherms are imaged in the CHIRP data as concordant, acoustically diaphanous strata with minimal lateral thickness variability. The CHIRP profiles, in areas with tectonically induced microtopographic offsets, reveal bioherm populations that are aligned parallel to the topographic offsets, with sediment fills in the intervening hangingwall lows onlapping the hangingwall, and smothering less developed bioherms. The intervening

sediment shows bedforms (Figure 11) and is assumed to be within wave base.

4.2 | Microbial bioherm features and surrounding sediment

In the south arm, the sublittoral bioherms investigated by diving and video between Bridger Bay and Promontory Point are both located east of the EGSL fault, on the footwall fault block (Figure 10, Figure S1). Side-scan sonar data reveal that bioherms are generally absent in the hangingwall block of the fault (Figure 10). These sublittoral bioherms have circular metre-scale shapes clustered together with convex-upward tops and a relief with respect to the lake bottom of 0.1–0.2 m, in some cases several decimetres (Figures 9 and 12A through D; Table 1; Figures S2 through S6). The surface of the bioherms consists of a 1–10 mm thick microbial mat, the top of which is brown to dark orange in colour with abundant *Ephydra* brine fly larvae attached (Figure 12A through D); the base of the millimetre-thick mat shows a dark to light green colour (Figure 12A,B). Carbonate precipitates occur just below the surficial microbial mat and consist of light grey to white millimetre to centimetre-size irregular patches locally mimicking faint lamination; 10–20 mm below the surficial microbial mat, dark grey to black laminae of precipitated carbonate can occur (Figure 12A,B). The surrounding sediment, locally rippled, consists of mud, ooids, detrital terrigenous grains and centimetre-size irregular aggregate grains and bioherm intraclasts, and organic debris (e.g. dead brine shrimp and brine fly larvae).

The bioherms in the north arm are white and not populated by either surface-based microbial mat or macro-invertebrate grazers (Figure S5). These bioherms exhibit less surface roughness and are surrounded by detrital siliciclastic sand grains and mud. Deposits of bioherm-derived intraclasts and detritus adjacent to the bioherms are conspicuously absent.

In the south arm bioherms, the dominant carbonate precipitates are aragonite associated with calcite, rare dolomite and halite. Dolomite was identified only in Promontory Point bioherms through XRD analysis (Figures S7 and S8) and SEM observation. Possible authigenic silicate minerals were observed through petrographic (Figure 13A) and SEM-EDS analyses.

The precipitated carbonate fabrics (Table 1, Figures 13 and 14; Figures S9 through S11) are similar in bioherms from different localities and water depths and occur as millimetre to centimetre-size patches irregularly distributed within the microbialite framework with pockets of internal sediment made of peloids and brine shrimp faecal pellets and cysts, ooids, brine fly larval cases, and rare diatoms, ostracods and gastropods. Peloidal internal sediment and brine shrimp cysts are more abundant in sublittoral bioherms with respect to
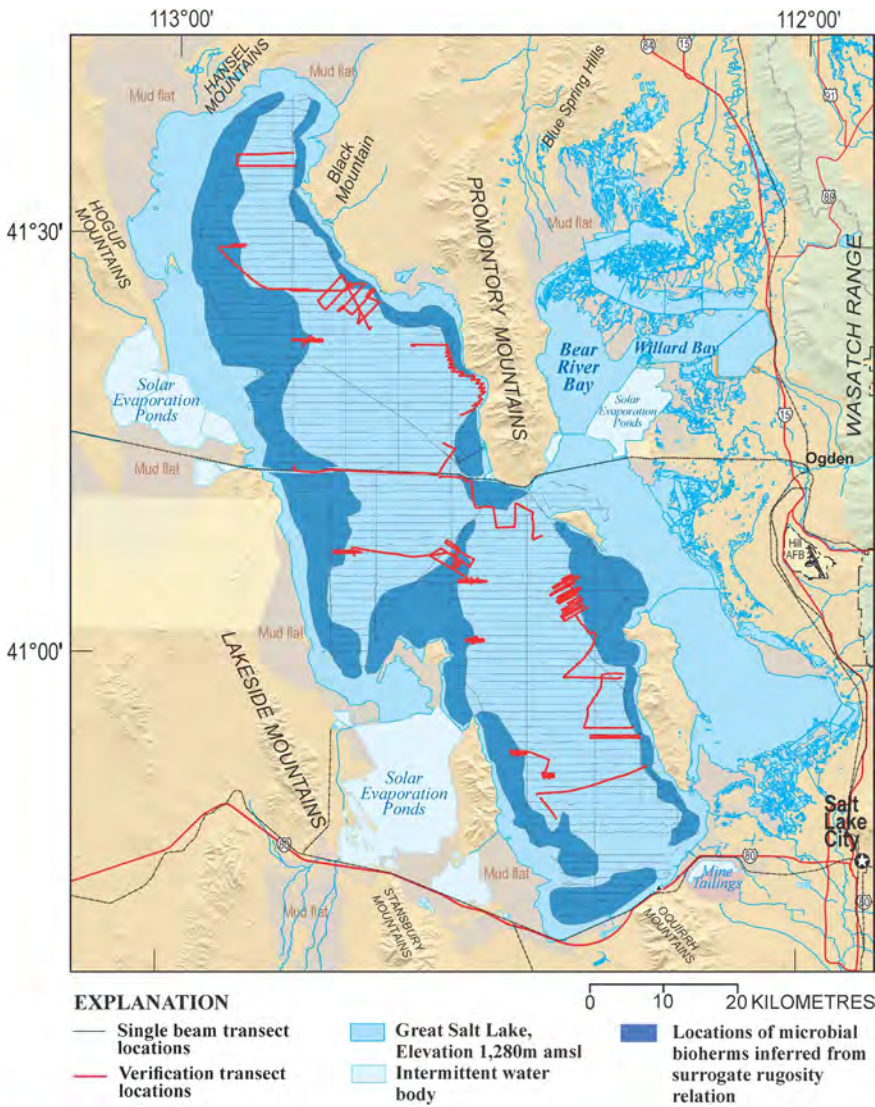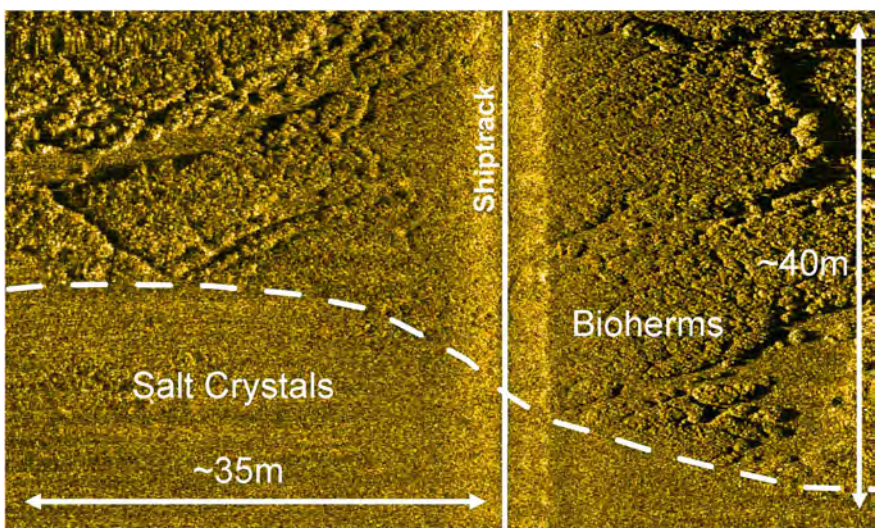
FIGURE 8 Side-scan sonar image shows obscured bioherm morphology in deeper waters of the north arm of GSL. Salt crystals precipitate from the high salinity water and cover most of the lake bottom. Waves and currents remobilise salt crystals deposited in shallow areas lakeward to deeper water

the shoreline ones. The three distinguished carbonate fabrics summarised in Table 1 are: (a) leiolitic to clotted peloidal micrite boundstone made of micrite-grade microcrystalline aragonite (Figure 13A through D); (b) sinuous threads of fibrous spherulitic boundstone consisting of equant to radially oriented fibrous aragonite crystals (10–100 μm long) forming

FIGURE 9 Image showing nearshore occurrence of microbial bioherms along the south-west margin of the south arm of GSL that were excluded from the total estimate of occurrence due to shallow water conditions. Occurrences such as these are located within the vertical range of modern lake levels and are subject to periods of submergence and exposure, physical weathering, and extreme temperature fluctuations. Bioherm in foreground is *ca* 1 m in diameter at lake level. View is from south-west looking east toward Antelope Island. Image from 2005 06 05. Lake surface elevation 1,277.9 m amsl
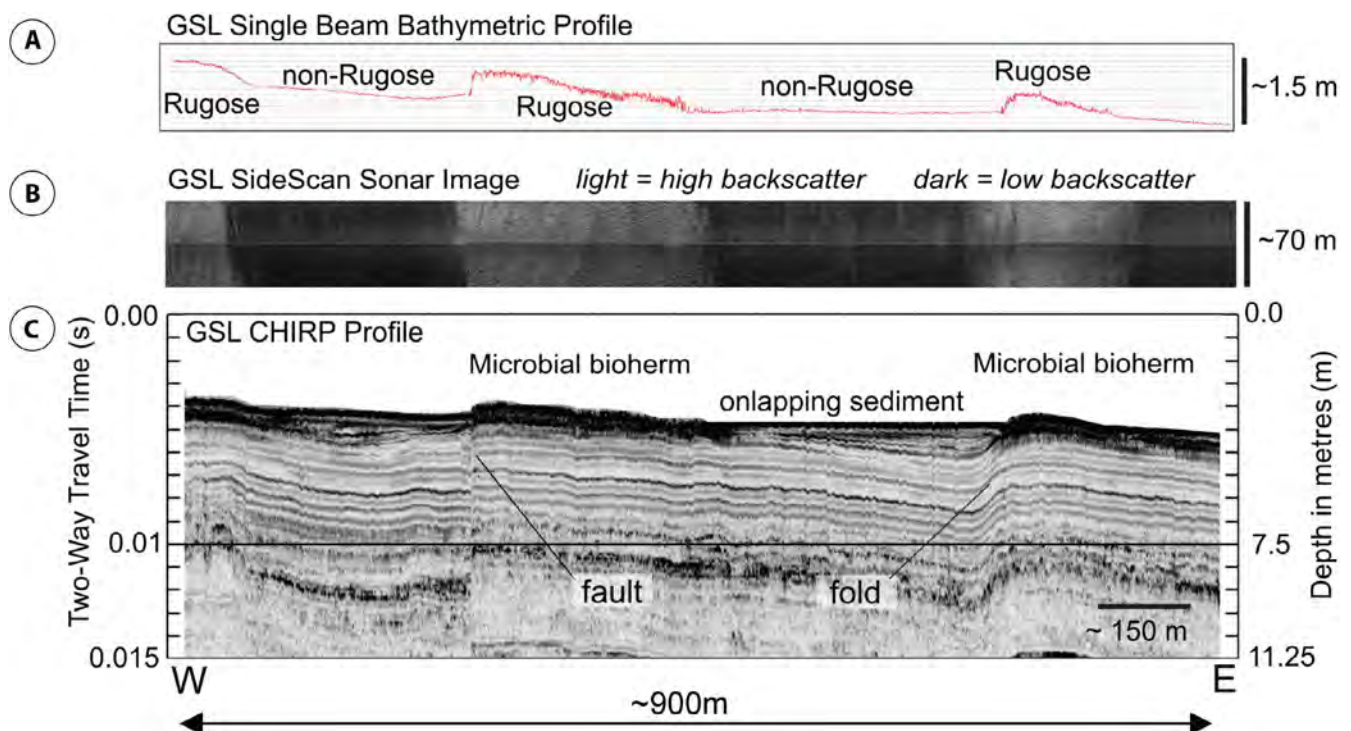
FIGURE 10 Relationship between benthic rugosity, microbial bioherm occurrence and tectonically induced microtopographic offsets along the western margin of the main body of GSL. (A) Single-beam bathymetry showing variations in roughness and depth associated with microbial bioherm occurrence. (B) Side-scan mosaic across a subset of varying rugose/non-rugose data showing three microbial bioherm deposits (lighter areas) and intervening lows (darker areas). The intervening lows are infilled with onlapping sediment and exhibit less backscatter. (C) CHIRP seismic profile co-registered with side-scan sonar image illustrates structural control on the topographic highs. Both the fault and fold show growth with depth

spheres around a micrite-grade nucleus (Figures 13C,E and 14A through E); these spherulitic structures are clustered together or form elongated irregular shapes; the outer terminations of the spherulitic structures are often lined by 20 μm thick limpid isopachous fibrous aragonite cement (Figure 13E,F); (c) laminated micritic boundstone are rare
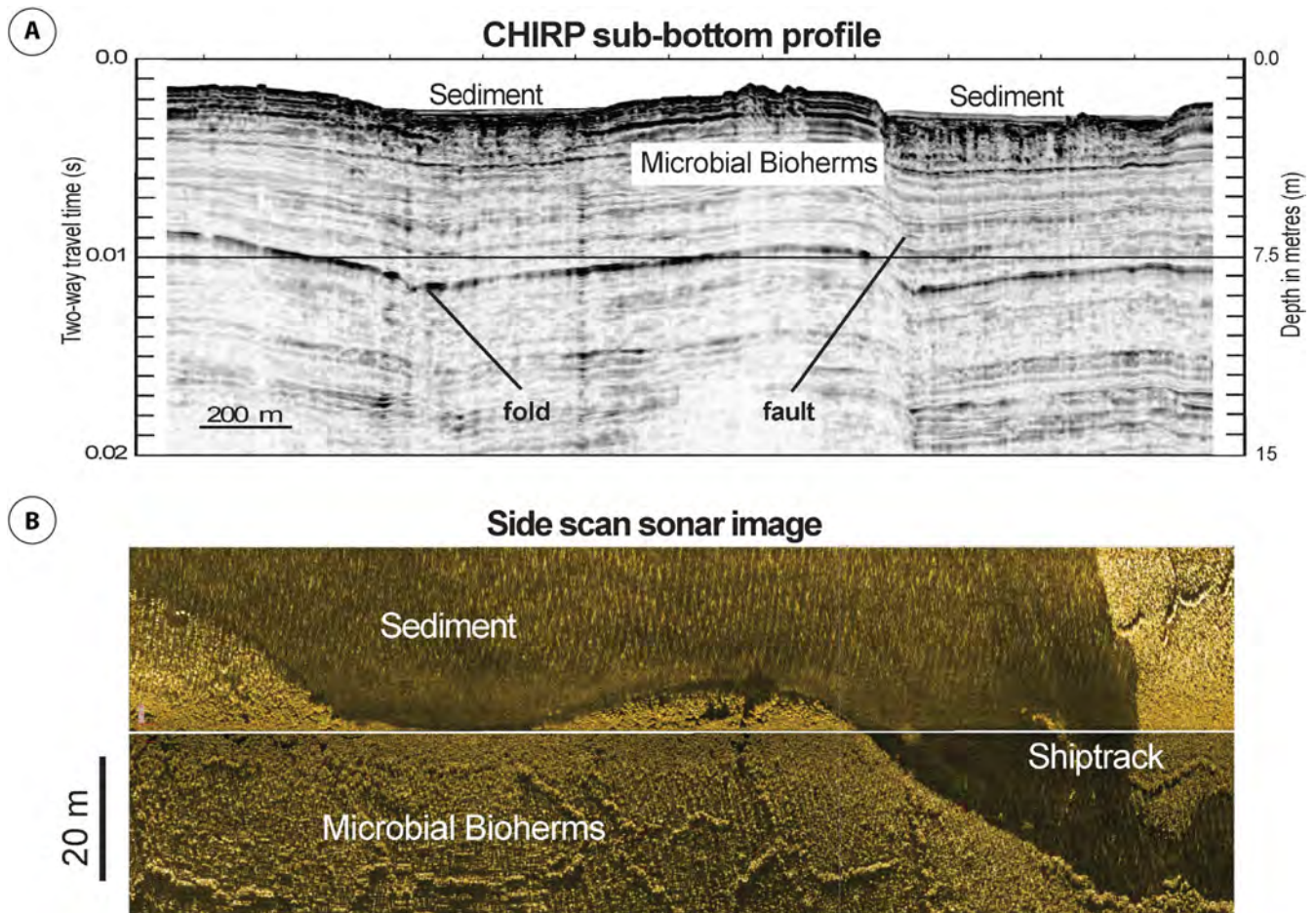
FIGURE 11 Relationship between sublittoral microbial bioherm exposure, tectonically induced microtopographic offsets, sediment deposition and microbial bioherm occurrence along the northern margin of the south arm of GSL. (A) CHIRP geophysical data south-west of Promontory Point showing finer-grained sediment covering previously exposed bioherms in depressions related to recent tectonism. (B) Side-scan sonar image collected concurrently with the CHIRP data showing sediment deposition in tectonically induced microtopographic lows. Image date 30 August 2009

but present towards the top of the bioherms exposed at the shoreline (Figure 14B), forming also centimetre-size columnar structures, which may be overlain by clotted peloidal micrite-grade boundstone.

Adjacent to the bioherms, millimetre to centimetre-size aggregate grains and bioherm intraclasts made of the same fabric types form sediment carpets (Table 1; Figure 14C,E). These grains also include green authigenic aluminium silicate (Figure 14E) as observed in the bioherms. The bioherm-derived intraclasts are more abundant surrounding the bioherms temporarily exposed at the shoreline rather than the sublittoral ones; in Bridger Bay they represent the transitional zone from the bioherm-dominated areas and the ooidal sand dominated shoreline area.

In cathodoluminescence, the bioherm-clotted peloidal micrite and the spherulitic boundstone often exhibit bright luminescence, whereas the fibrous isopachous cement is non-luminescent (Figure S10). Ooids (Figure 14F) show variable fabrics ranging from radial fibrous, tangential, superimposed radial to tangential fabrics or vice versa (Table 1) and are non-luminescent, whereas peloids at ooid nuclei and outermost micrite-grade cortex of the ooids can show bright luminescence.

The analysis at SEM of the bioherm carbonate precipitates (Figure 15A through L) shows that organic substances are ubiquitous overlying and surrounding the mineral precipitates. This organic matter shows alveolar textures and represents microbial biofilm extracellular polymeric substances (EPS), which, in some cases, display enrichment in Si, Mg, P, Al and Fe when analysed through EDS. At the micron-scale carbonate precipitates consist of: (a) fibrous aragonite crystals (5–20 μm in length) with hexagonal or squared cross-section randomly oriented (Figure 15A) or organised in radial spherulites with diameters of 10–100 μm (Figure 15D,E); (b) micrite-grade (micron to submicron nanometre-scale) sub-spherical structures of carbonate (0.1–1 μm) embedded in or overlying EPS (Figure 15A through C,F) and forming irregular aggregates or peloids with diameters tens of microns
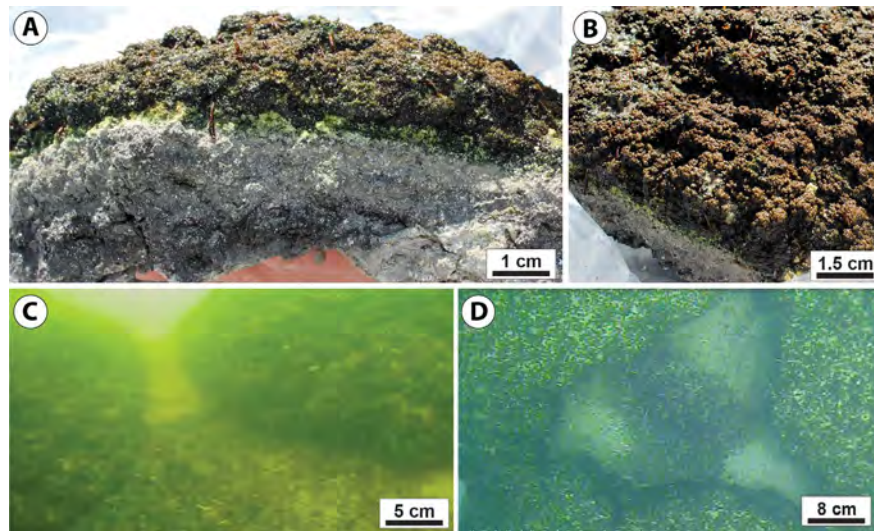
FIGURE 12   Sublittoral microbial bioherms from the south arm. (A and B) Hand samples of sublittoral bioherms capped by a centimetre-thick microbial mat: brown to dark orange colour at the top and dark to light green on the lower surface at the contact with the precipitated carbonate. The light grey carbonate precipitates form a patchy framework and include dark grey to black sub-horizontal faint laminae, 10–20 mm below the basal surface of the microbial mat. (C and D) Photographs of sublittoral bioherms with convex-upward shape, decimetre high relief and surficial microbial mat with brine fly larvae attached. Bioherms are surrounded by ooids and bioherm-derived intraclasts and aggregate grains

wide; (c) 5–10 μm rhombohedral calcite crystals formed by the coalescence of micron to nanometre-scale carbonate sub-spherical carbonate structures (Figure 15G). These precipitates occur associated with halite, rare dolomite, framboidal pyrite and diatoms (Figure 15K,L). Rare filamentous microbes have been observed through SEM (Figure 15H,I). Fibrous aragonite crystals form cement growing into open pores and nucleating on micrite-grade sub-spherical carbonate structures (Figure 15J).

5 | DISCUSSION

5.1 | Rugosity and controls on microbial bioherm spatial distribution

By comparing patterns and degree of rugosity with acoustic returns from known benthic environments, a surrogate relationship was developed to identify occurrences of microbial bioherms throughout the navigable extent of GSL. Results of both the Moran's *I* and Getis-Ord Gi* statistics reject the assertion that rugosity in GSL is randomly distributed. As such, the non-random spatial distribution of rugosity indicates that at least one factor, such as depth, aspect, or salinity, influences the distribution of benthic rugosity and the benthic forms that may be causing that rugosity.

Side-scan sonar with visual confirmation of bioherm occurrence verified the surrogate relationship between increases in rugosity and bioherm occurrence. On every transect, changes in benthic rugosity were correlated with an analogous change in microbial bioherm occurrence. The GSL bioherms occur as structures with positive relief and vary from dispersed to laterally connected coalesced assemblages throughout shallow areas of the lake. Clustering of bioherm populations, to the point of forming continuous laterally connected coalesced deposits shoreward of each occurrence, indicates that changes in depth, or some environmental variable related to depth, such as finer-grained sediment deposition, light availability, wave or current-related energy, or a combination of factors, have an effect on bioherm initiation, growth, survivability and preservation. As depth increases, bioherm populations become increasingly sparse, reaching an elevation (*ca* 1,273.7 m amsl) beneath which occurrences of bioherms, if they exist, are no longer identifiable using the rugosity surrogate method or side-scan sonar.

The pre-causeway (pre-1960s) extent of microbial bioherms exposed at the sediment/water interface in GSL probably significantly exceeded the approximately 1,000 km^2 extent verified during this investigation. This estimate is more than four times the 1938 estimate of Eardley (approximately 259 km^2), and the actual areal extent of microbial bioherm occurrence in GSL is probably larger due to survey and methodology limitations. In fact, deposits of recent sediment in the south arm of the lake also may mask additional bioherm occurrences, especially in high sediment inflow areas along the eastern margins of the south arm of the lake (Figure 9).

Quantification of change in population distributions along the observed gradient was not possible as not all individual bioherms within clustered populations could be identified. In some areas, a pavement of continuous intergrowth of bioherms was apparent in the side-scan sonar imagery. Complications in identifying individual bioherms within

TABLE 1 Summary description of identified carbonate facies in Great Salt Lake

Facies types	Spatial distribution	General features	Precipitated fabric types	Description	Cement types and other diagenetic features	Porosity
Bioherms	Convex-upward to flat horizontal domes with circular to oblate cross-section (isolated 0.2–2 m in diameter; clusters up to 10 m in diameter; *Bridger Bay*) or lensoid perpendicular to shorelines (0.2–4 m wide, 1 m to several metres long; those exposed on the shoreline show 10 cm raised rims and concave-upward top filled by rippled ooidal sand in the centre; *Promontory Point*). Mean bioherm relief with respect to surrounding sediment: 10–20 cm to tens of dms (up to 1–1.5 m) for those at water depth of 3–4 m. Bioherms form belts subparallel to the shoreline for several km extending from 10 s to 2–3 km	*Outer surface*: 1–5 mm to 1 cm thick brown to dark orange at the top, dark to light green at base, microbial mat with brine fly larvae attached. *Internal structure*: mm to cm size irregularly distributed patches of different fabric types (1 clotted micrite, 2 fibrous spherulitic boundstone, 3 laminated micritic boundstone) and internal peloidal sediment	1 Leiolitic to clotted peloidal micrite boundstone	Structureless micrite-grade microcrystalline carbonate with sparse clots and peloids (20–100 μm in diameter) or peloids of 10–60 μm surrounded by 20–50 μm crystals	*Mineralogy*: aragonite, calcite, rare dolomite, halite, authigenic green aluminium silicate and detrital minerals.	Depositional framework porosity (0.05–1 mm pore size); interlaminae porosity; microporosity; interparticle porosity.
			2 Sinuous threads of fibrous spherulitic boundstone	Patches (mm to cm size) of a framework of sinuous threads of sub-spherical structures (100–200 μm in diameter) made of equant crystals or radially oriented fibrous (spherulitic) aragonite crystals (10–100 μm long) around a micritic nucleus. The outer terminations of the spherulitic structures are lined by 20 μm thick limpid fibrous aragonite cement	Green silica-rich material associated with outer microbial mat. Early diagenetic isopachous cement fringes of fibrous aragonite (20–50 μm thick) lining primary pores.	Biomouldic porosity from brine shrimp cysts
			3 Laminated micritic boundstone	Structureless leiolitic or peloidal laminae, 0.1–1 mm thick, forming layers a few mm to 2–3 cm in thickness. Laminae form upward-oriented columnar structures, commonly 5–10 mm wide and 0.5–1.5 cm high, but also 5 cm high and 5–8 cm wide. Laminated boundstone occurs towards the top of bioherms; it may be overlain by 1–2 cm of clotted micrite boundstone. Some laminated columns have a clotted peloidal nucleus; others surround patches of spherulitic boundstone		
			Surrounding and internal sediment within precipitated fabrics in mm to cm size pockets	Peloids and brine shrimp faecal pellets (50–600 μm to 1 mm), brine shrimp cysts, ooids, detrital quartz, feldspars and lithic fragments from metamorphic and igneous rocks. These grains form grainstone, packstone to wackestone with interparticle fibrous isopachous cement or structureless micrite. Bioherms are surrounded by these grain types associated with spherulitic aggregate grains and bioherm-derived intraclasts		

TABLE 1 (Continued)

| Facies types	Spatial distribution	General features	Precipitated fabric types	Description	Cement types and other diagenetic features	Porosity
Irregular spherulitic aggregate grains and bioherm-derived intraclasts	Sand and gravel-size grains made of spherulitic aggregate grains, bioherm-derived intraclasts and ooids surround the bioherms forming cm to dm-thick sheets. These grains also form the transitional zones between the bioherm-dominated and the ooid dominated zone along the shorelines	From 1 mm to 2 cm in diameter. These grains include all the precipitated fabrics observed in the bioherms (1, 2, 3) and trapped peloidal ooidal packstone/wackestone with detrital grains. They are coated by same green microbial mat as the bioherms	Dominated by irregular sinuous threads of fibrous spherulitic boundstone but include also structureless micrite-grade laminae and patches of clotted peloidal micrite	Spherical bodies (50–200 μm in diameter) consisting either of fibrous sinuous threads or of a nucleus of micrite lined by aragonite fibrous crystals. These sub-spherical structures are surrounded by dense and clotted peloidal micrite. Trapped grains are peloids, ooids, detrital quartz and micas	*Mineralogy*: aragonite, calcite, halite, authigenic green aluminium silicate and detrital clay minerals. Green silica-rich material associated with outer microbial mat. Rare early diagenetic, fibrous aragonite isopachous cement fringes lining primary pores	Interparticle; intraparticle; framework porosity (0.05–1 mm pore size); microporosity
Unlithified ooidal sand and lithified ooidal grainstone beachrock	Belts nearly 2–6 km wide subparallel to shorelines from exposed subaerial beach and aeolian dunes to subaqueous strandline	*Ooid size*: average 300–400 μm in diameter, size range 0.2–1 mm. *Ooid nuclei*: detrital quartz and feldspar grains, peloids (50–200 μm in diameter). *Aggregate ooids*: bound together with bioherm intraclasts by meniscus micrite	Radial ooids	Cortex: acicular to bladed (20–200 μm long) aragonite crystals departing perpendicularly away from the nucleus. Radial ooids may show growth lines but no micrite-grade laminae. Radial concentric ooids show concentric micrite-grade laminae alternating with fibrous crystal growth lines	Pendant and meniscus calcitic microsparitic/micritic cement of vadose meteoric diagenesis in beachrock ooidal grainstone	Interparticle; intercrystalline; microporosity. Secondary mouldic (oomouldic in beachrock)
			Tangential ooids	Cortex: concentric laminae micrite-grade to fine crystalline <10 μm thick		
			Radial to tangential ooids	Ooids with mixed crystal fabric starting as radial (100–150 μm thick) around the nucleus overlain by tangential coating (100–150 μm thick)		
			Tangential to radial ooids	Ooids with mixed crystal fabric starting as tangential around the nucleus (100–150 μm thick) overlain by radial fibres coating (100–150 μm thick)		
			Random fibres orientation lacking nucleus	No nucleus; fibrous to equant aragonite crystals randomly oriented and separated by irregular patches of micrite-grade microcrystalline aragonite		
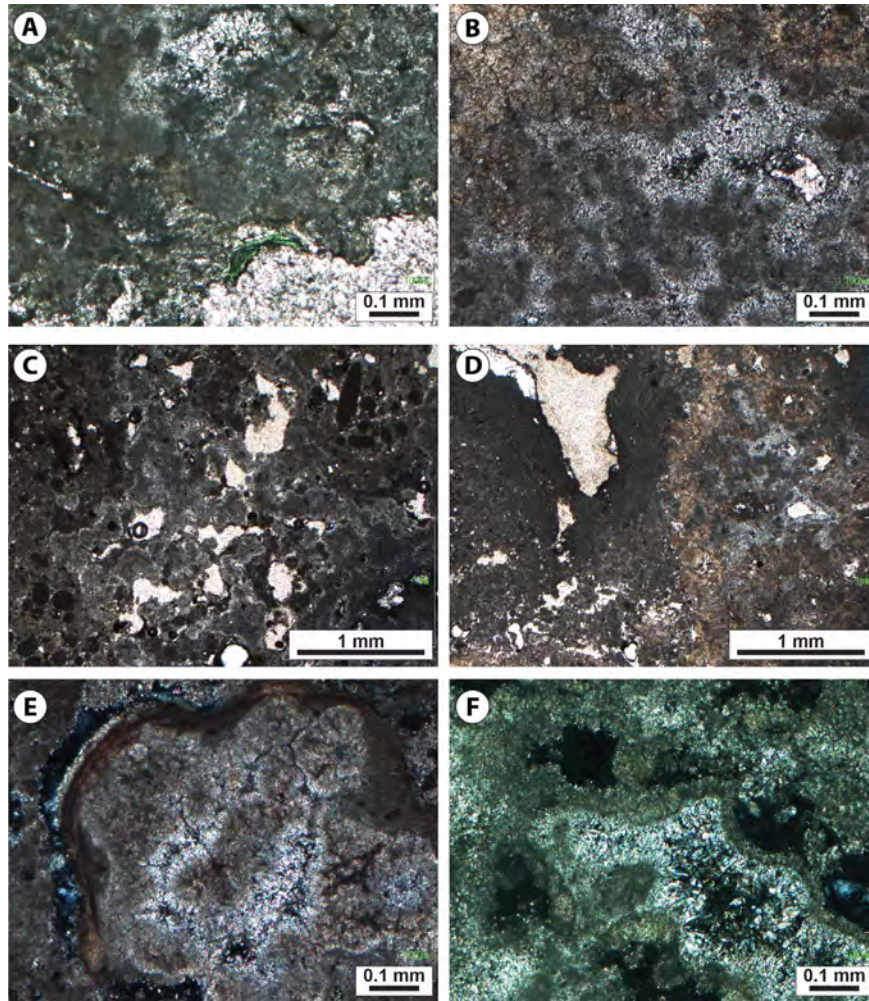
FIGURE 13 Photomicrographs of microbial bioherm carbonate fabrics. (A) Clotted peloidal micrite boundstone showing in the lower part a green mineral representing possibly an authigenic aluminium silicate as suggested by the chemical composition analysed through SEM-EDS. (B) Area with clotted peloidal micrite with framework porosity filled by fibrous aragonite cement; in the upper part clotted micrite-grade aragonite is transitional into the sub-spherical structures (100 μm in diameter) made of spherulitic fibrous crystals. (C) Sinuous threads of fibrous spherulitic boundstone with open framework porosity surrounded by internal sediment with peloids and faecal pellets. (D) Columnar structure made of clotted peloidal micrite with fibrous aragonite cement filling framework porosity, followed by sinuous threads of fibrous spherulitic boundstone draped by leiolitic micrite-grade structureless carbonate. (E) Close-up view of sub-spherical spherulitic structures with fibrous aragonite cement overgrowth. (F) Image in crossed polarizers showing the isopachous fibrous aragonite cement lining framework porosity within the microbial clotted peloidal micrite-grade boundstone

clustered populations included variations in bioherm size, degree of interconnectivity, possible burial by sediment, acoustic shadows masking adjacent bioherms. Distortions due to georectification, probable variations in sound velocity within the lake, and onlapping sediment masking bioherm occurrence also inhibited quantification of distributions within the larger surveyed populations. Statistically dispersed populations were quantified in areas down-gradient of clustered shallow water occurrences due to the separation and acoustic reflectivity of individual bioherms in those areas.

The general absence of microbial bioherms below an elevation of *ca* 1,273.7 m amsl in the south arm of GSL may indicate a persistent or recurring pycnocline (chemocline or thermocline) preventing initiation, development, survival,

preservation, or a lack of suitable environmental conditions for their survival. The depth difference between bioherm occurrence and non-occurrence could also be related to wave or current energy, sediment deposition in the profundal zone, or light extinction. Although a persistent hypersaline layer currently forms in the south arm of the lake, its occurrence is tied to differences in lake elevation between the restricted north arm and the south arm, and contributions of high-salinity water migrating through the rock-filled causeway into the south arm. Data are not available that indicate a persistent pre-causeway pycnocline existed prior to the rock-filled causeway, however, one could have existed.

In the north arm of GSL, the accumulation of halite and other evaporative minerals in the deeper sections of the lake

FIGURE 14 Photomicrographs of microbial bioherms, bioherm intraclasts surrounding the bioherms and ooids. (A) Framework made of sinuous threads of spherulitic structures surrounded by wackestone with ooids and peloids embedded in leiolitic micrite-grade carbonate. (B) Laminated micrite draping spherulitic boundstone. (C) Aggregate grains and bioherms intraclasts surrounding the bioherms made of spherulitic boundstone associated with ooids and faecal pellets. (D) Close-up view of bioherm intraclast made of spherulitic structures next to clotted peloidal micrite. (E) Spherulitic boundstone from bioherms intraclast with green mineral representing an authigenic aluminium silicate as indicated by SEM-EDS analyses. (F) Crossed-polarizers image of ooids showing radial fibrous and tangential fabric with nuclei made of detrital quartz grains
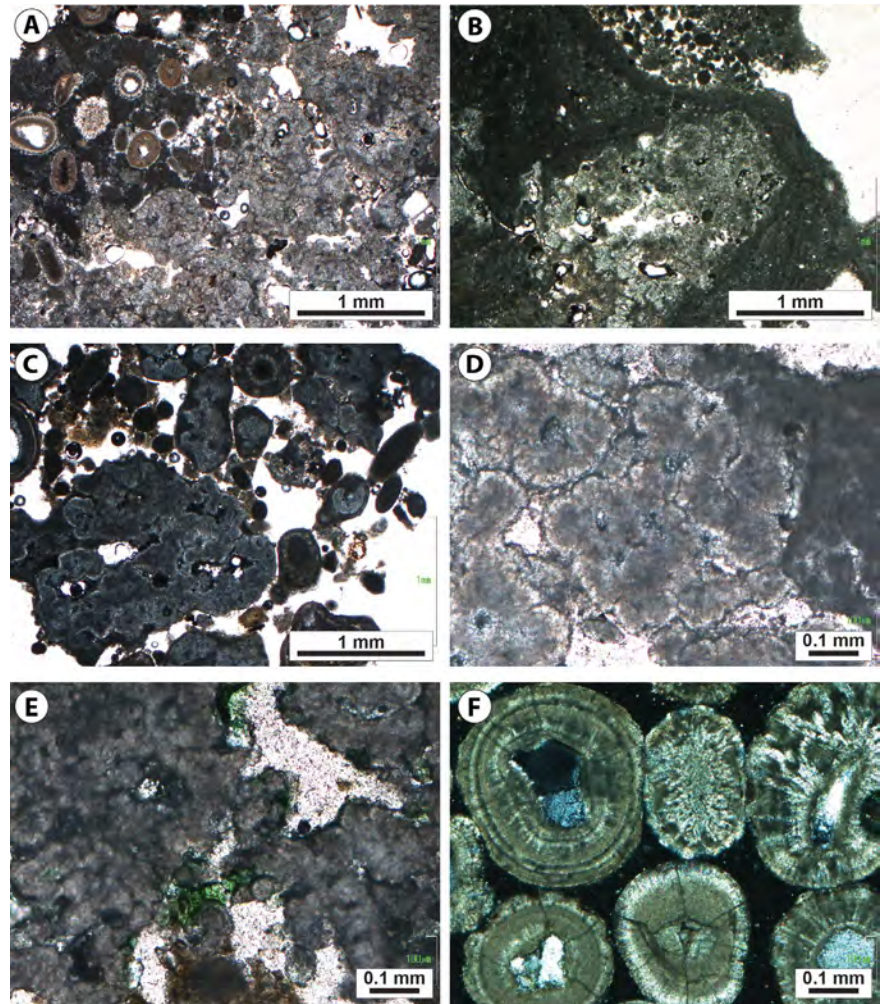
prevented identification of changes in microbial bioherm occurrence along a shallow to deeper gradient except in areas where wave energy and currents are suspected to mobilise and transport salts to deeper waters. These areas were limited to shallow, near-shore areas where shallow water and limited bottom visibility generally prevented verification of bioherm occurrence. Acoustically defined rugosity in sub-bottom geophysical data indicates that widespread occurrences of microbial bioherms existed in the north arm of GSL before the onset of extensive salt deposition.

The overprint of faults and folds on concordant, acoustically diaphanous strata with minimal variability in lateral thickness located directly under microbial bioherm occurrences suggests that tectonic activity occurred after a prolonged period of finer-grained sediment deposition, likely a profundal lacustrine environment related to Lake Bonneville. The occurrence of continuous laterally connected coalesced deposits of microbial bioherms along fault-related topographic highs is strong evidence that growth of the microbial bioherms initiated after the topographic highs started forming, as bioherms are not visible beneath the finer-grained sediment that infills the topographic lows. Small-scale (1–2 m) offsets resulting from tectonic events would subject

topographic highs to increased light availability and/or to the effects of greater wave or current energy that could remove finer-grained sediments and provide a stable base for bioherm initiation, prevent sediment deposition, or increase availability of nutrients. A combination of these factors could contribute to the apparent success of the larger, closely spaced bioherms found in these locations.

Towards the bases of the footwall ramps, bioherm distributions generally grade into finer-grained sediment and, in some cases, appear to be completely buried by onlapping sediment. This relationship between structural topographic highs associated with microbial bioherm occurrence and corresponding onlapping sediments trapped in hangingwall lows is consistent with observations from ancient Ediacaran microbialite deposits (Johnson & Grotzinger, 2006), which suggests lateral growth of microbialites is inhibited by sedimentation. The reduction in light availability, 'drowning' of the microbial communities mediating carbonate precipitation responsible for bioherm growth, or the lack of suitable initiation locations could all contribute to the lack of extensive bioherms in these areas and the observed patterns of microbial bioherm occurrence in GSL.

Observations of changes in bioherm size and density through the shallow to deeper water gradient suggest that
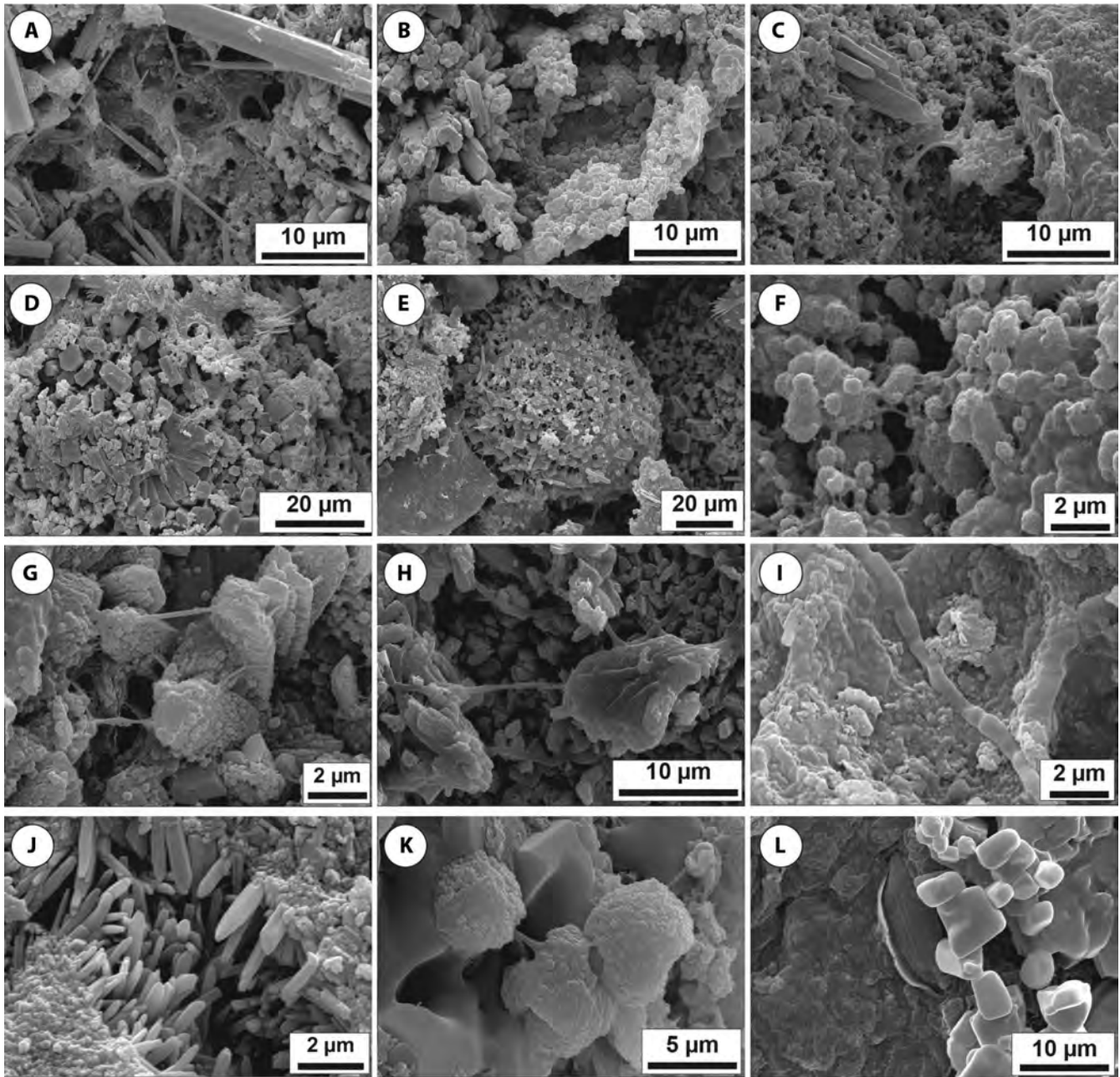
FIGURE 15 Images at SEM of microbial bioherms. (A) Alveolar texture often characterising microbial biofilm EPS embedding micrite-grade (sub-micron scale) carbonate precipitates and crossed by fibrous aragonite crystals. (B) Microbial biofilm EPS embedding micron and submicron-scale sub-spherical carbonate structures representing the micrite-grade clotted peloidal precipitates. On the left fibrous aragonite with hexagonal cross-section. (C) Organic substances deriving from biofilm EPS embedding micron and submicron-scale sub-spherical carbonate structures forming the clotted peloidal micrite-grade fabric. Fibrous aragonite crystals grow through the EPS with microcrystalline aragonite. (D) Fibrous aragonite spherulites overlain by micron-scale carbonate structures and microbial biofilm EPS. (E) Fibrous aragonite spherulites draped by organic material representing microbial biofilm EPS. (F) Carbonate precipitates made of sub-spherical micron to sub-micron scale structures connected by organic material. (G) Rhombohedral crystals made from the aggregation of nanometre-scale sub-spherical carbonate precipitates connected by organic substances. (H) Fibrous aragonite with hexagonal cross-section overlain by micrite-grade aragonite and possible filamentous microbes. (I) Possible filamentous microbe on biofilm EPS. (J) Aragonite fibrous cement growing into open pore space nucleating on clotted peloidal micrite-grade precipitates. (K) Sub-spherical structures made of rhombic crystals that might represent the dolomite identified through XRD analysis. (L) Microbial mat EPS on the left overlain by a pennate diatom and halite crystals on the right

it is not the faulting itself that controls the location of the bioherms but the changes in associated environmental conditions along that gradient. In an environment opposite of that found in shallower waters near the topographic highs, decreased light availability, less wave or current energy, fewer initiation surfaces, increases in finer-grained sediment

deposition, or a combination of these factors could account for decreasing bioherm populations and more dispersed populations. Areas absent of microbial bioherms are primarily in pelagial zones or along the margins of the lake where depth-related environmental factors or clastic deposition has prevented their formation or effectively masked their occurrence. The absence of microbial mats, including non-lithified forms, between the bioherms has been confirmed by direct observation.

Ring bioherms were not encountered in the sublittoral zone, supporting the view that they require some degree of exposure (Bouton et al., 2016a; Vanden Berg, 2019). This suggests that although lake levels have fluctuated significantly, if bioherms currently in the sublittoral zone have undergone significant exposure, they have annealed the effects of exposure. Not encountered were the ridge types described by Vanden Berg (2019) or the elongated lensoid deposits described by Carozzi (1962) from Promontory Point (Table 1, Figure S2), which show striking similarities to microbialites described from the Devonian lacustrine deposits from the Orcadian Basin in Scotland by Andrews and Trewin (2014); such morphologies appear to be more common on shallower wave influenced shorelines.

5.2 | Microbial bioherm mineralogy

The mineralogical composition of the sublittoral bioherms, the focus of this study, does not differ from the bioherms found adjacent to the present-day shoreline, implying that mineralogy cannot be used to differentiate environments. The predominance of aragonite precipitates associated with calcite and dolomite in GSL microbial bioherms and ooids as reported in this and previous studies (Della Porta, 2015; Dunham et al., 2020; Eardley, 1938; Ge et al., 2021; Pace et al., 2016; Pedone & Folk, 1996; Sandberg, 1975) is explained by the high carbonate supersaturation and Mg/Ca ratio of lake water, which is between 9.6 and 115.7 (cf. Müller et al., 1972). Pedone and Dickson (2000) interpreted dolomite formation as a replacive, fabric-preserving product in the study of 12 ka old microbialites from Stansbury Island. They suggested that dolomitization occurred during the Gilbert transgression (11–10 ka), when the mounds were submerged for an extended period of time. Dolomite was not biologically mediated but formation of the crystal core by bacterial mediation followed by abiotic growth of the crystals could not be ruled out (Pedone & Dickson, 2000). Pace et al. (2016) suggested that dolomite forms from the partial dissolution and replacement of microbially mediated aragonite, driven by sulphate-reducing bacteria degrading cyanobacteria biofilm in slightly acidic pore water. Comparably, Dunham et al. (2020) proposed that the activity of sulphate-reducing bacteria promotes proto-dolomite precipitation in mildly acidic microenvironments and aragonite dissolution due to fermentation-derived acidity.

In GSL microbial bioherms, most of the organic matter surrounding the carbonate precipitates is enriched in Si, Al, Mg and Fe suggesting that possibly amorphous silicate phases are preferentially associated with biofilm EPS as observed in various studies about recent microbial carbonates (Arp et al., 2003; Benzerara et al., 2010; Bontognali et al., 2010; Burne et al., 2014; Jaramillo-Vogel et al., 2019; Jones & Peng, 2014; Kremer et al., 2019; Martín-Pérez et al., 2021; Perri et al., 2018; Zeyen et al., 2017). This is confirmed by Pace et al. (2016) who identified a Mg-Si phase, close to sepiolite or stevensite, nucleating on the microbial extracellular organic matrix due to increased pH driven by coccoid cyanobacteria photosynthesis followed by aragonite precipitation. In the Abu Dhabi sabkha, spheroids of primary dolomite form within EPS, which show an alveolar structure rich in Mg and Si, with almost no Ca (Bontognali et al., 2010). It is suggested that the ability of EPS to preferentially bind Mg and Si might play an important role in overcoming the kinetic barrier that prevents the nucleation of dolomite at low temperature (Bontognali et al., 2010).

5.3 | Microbial bioherm fabrics and precipitation processes

Vennin et al. (2019) investigated in detail the Bonneville and GSL microbial carbonates deposited along exposed palaeo-shorelines (30 to 11.5 ka) and from 11.5 ka to present-day, evaluating the controls on microbialite morphological features and composition linked to lake level and climate fluctuations. Carbonate production is suggested to be controlled by the interaction of physical (kinetics of the mineral precipitation, lake water temperature and runoff), chemical (Ca^{2+}, Mg^{2+} and HCO_3 concentrations, Mg/Ca ratio, dilution and depletion) and/or biological (trophic) factors. Vennin et al. (2019) distinguished four macrofabrics in GSL microbial bioherms (cow-pie, domes and columns, oncoids, mimetic substrate crusts), two mesofabrics (clotted, laminated) and four microfabrics. The described microfabrics consist of: (a) peloids associated with 'intestine-like' fabric dominated by aragonite, as labelled in Pace et al. (2016); (b) coccoids organised in clusters; (c) micritic laminae; and (d) filaments related to poorly preserved fossil moulds.

Domes and columns sensu Bouton et al. (2016a) and Vennin et al. (2019) correspond to the sublittoral bioherms described in this study. The oncoids match the irregular spherulitic aggregate grains and bioherm-derived intraclasts observed in this study in between bioherms and forming carpets transitional to ooidal sand in Bridger Bay. These grains made of spherulitic structures were labelled as pustular grains or microbial popcorn by Chidsey et al. (2015). The four

microfabrics described by Vennin et al. (2019) are similar to those identified in this study with the coccoids and peloids corresponding to the clotted peloidal micrite-grade boundstone, the intestine-like fabric corresponding to the sinuous threads of spherulitic boundstone and the equivalent laminated microfabrics. Chidsey et al. (2015) described the relic bioherms at Rozel Point in the north arm as made of pustular thrombolites in the inner portion and laminated stromatolites near the surface. Open primary constructional pores are common within the microbial structures and are lined by acicular radial cement (Chidsey et al., 2015).

Della Porta (2015) suggested that carbonate precipitation might result from a continuum of physico-chemical and microbially induced and influenced processes (sensu Dupraz et al., 2009) due to the combination of supersaturated hypersaline lake water and the ubiquitous presence of microbial biofilms acting as substrate for carbonate mineral nucleation. The clotted peloidal and laminated micrite-grade fabric observed petrographically resemble the textures interpreted as microbial boundstone in several studies about recent and fossil microbialites. Nanometre-scale sub-spherical carbonate structures eventually coalesce to form larger crystals with rational/euhedral crystal faces as similarly described in studies about microbially mediated carbonate precipitation (Bontognali et al., 2010; Ge et al., 2021; Jones, 2017; Jones & Peng, 2014; Pedley, 2014; Pedley et al., 2009; Perri et al., 2012, 2018). Meldrum and Cölfen (2008) have shown that several biominerals of skeletal organisms can form from amorphous precursors represented by nanoparticles, which are favoured by supersaturation. In fact, biogenic carbonate precipitation often proceeds via a transient amorphous calcium carbonate (ACC) precursor phase (Jones, 2017).

Pace et al. (2016) proposed a model explaining the formation of GSL microbial bioherms consisting of three steps related to geochemical gradients driven by microbial metabolism: (a) a poorly crystallized Mg-Si phase forms on the alveolar extracellular organic matrix due to increased pH over 10, because of active coccoid cyanobacteria photosynthesis; (b) aragonite nucleates due to sulphate reduction during degradation of cyanobacteria biofilm by sulphate-reducing bacteria with intestine-like aragonite nucleating inside coccoid clusters, expanding in the extracellular organic matrix and embedding the Mg-Si phases; (c) dolomite partially replaces aragonite in neutral to acidic pore water through dissolution of aragonite and precipitation of dolomite at the interface between extracellular organic matrix and aragonite-Mg-Si phase patches. Pace et al. (2016) highlighted the critical role played by sulphate-reducing bacteria degrading EPS and cyanobacteria biofilm as demonstrated in other studies on recent microbial carbonates (Dupraz et al., 2004, 2009 and references therein; Baumgartner et al., 2006; Dupraz & Visscher, 2005). Pace et al. (2016) also proposed that the precursor

Mg-Si phase is instrumental for the nucleation and growth of aragonite crystals.

Lindsay et al. (2017) performed detailed microbiological analyses of GSL microbial mats both in the south and north arm establishing that the microbial community includes halophilic archaea, heterotrophic bacteria (the common polysaccharide-degrading bacterium *Marinimicrobium haloxylanilyticum*) and cyanobacteria. Cyanobacteria are abundant in the south arm and consist of the halophilic cyanobacterium *Euhalothece* sp., probably corresponding to *Aphanothece* identified by Reitner et al. (1997) and Wurtsbaugh et al. (2011) (cf. Lindsay et al., 2020). Lindsay et al. (2017) suggested that the fibrous aragonite crystals precipitated abiotically, whereas micrite-grade aragonite precipitation was driven by photoautotrophs such as the cyanobacteria *Euhalothece* and diatom *Navicula* that were responsible for mediating aragonite precipitation by inducing an increase in alkalinity through photosynthesis. The lack of this photosynthesizing community in the north arm due to the high salinity indicates that the north arm microbialites are relic remnant structures and present-day carbonate precipitation in the north arm is primarily abiotic (Lindsay et al., 2017, 2019). Lindsay et al. (2020), still attributing a key role to cyanobacteria photosynthesis in inducing aragonite precipitation, discussed the possible mediation of carbonate precipitation by sulphate-reducing bacteria as earlier published by Pace et al. (2016). The revised model by Lindsay et al. (2020), integrating the dolomite precipitation mechanism proposed by Dunham et al. (2020), suggests that cyanobacteria photosynthesis induces an alkalinity increase that promotes aragonite precipitation. Phototroph biomass supports a heterotrophic bacterial community with anaerobic fermentative bacteria that induce a decrease in pH and promotes the partial dissolution of aragonite and provide organic acids to support sulphate-reducing bacteria (Dunham et al., 2020; Lindsay et al., 2020). The activity of sulphate-reducing bacteria drives an increase in alkalinity that allows for the formation of proto-dolomite from the partial dissolution of aragonite (Dunham et al., 2020).

Following extensive investigation in moderate to high alkalinity settings, Arp et al. (1999a, 1999b), Arp et al. (2001, 2003) proposed that in such physico-chemical conditions, CO_2 removal by cyanobacteria photosynthesis appears to be of secondary or negligeable importance in raising supersaturation sufficiently to drive carbonate precipitation, because of the large DIC (dissolved inorganic carbon) pool and pH buffering. Nevertheless, cyanobacteria produce copious amounts of EPS that initially prevent carbonate precipitation by binding Ca^{2+} ions. When the EPS inhibiting capacity is surpassed by an excess supply of Ca^{2+} and by EPS degradation, precipitation of microcrystalline carbonate can occur randomly distributed within the exopolymeric substances without spatial relationships with cyanobacteria

cells. Conversely, cyanobacterial sheath calcification induced by photosynthesis most likely occurs in weakly pH-buffered waters, low in DIC and high in Ca^{2+} (Arp et al., 2001, 2002).

In this study, microbial bioherm petrographic and SEM observations have shown that micron and nanometre-scale aragonite precipitated on EPS is not linked to cyanobacteria cells and carbonate precipitates are absent from the surficial cyanobacteria-rich microbial mat. Hence, it is more likely that carbonate precipitation is influenced by the nucleation capacity of degrading EPS (cf. Arp et al., 1999a, 1999b; Arp et al., 2003) and by sulphate reduction as earlier proposed by Reitner et al. (1997) and Pace et al. (2016). In fact, 1–2 cm below the bioherm top surface covered by the unlithified microbial mat, there are laminae of black coloured carbonates suggesting sulphate reduction.

As highlighted by Lindsay et al. (2020), the remnant microbialites in the GSL north arm might be related to high salinity that prevented the proliferation of cyanobacteria. Nevertheless, an alternative explanation for the north arm relic bioherm might be that sulphate-reducing bacteria are also salinity limited and the lack of cyanobacteria microbial mat in the north arm might reduce the presence of heterotrophic sulphate-reducing bacteria that need photosynthate to support their metabolic activity (Lindsay et al., 2020).

5.4 | Implications of the research for environmental management and geological interpretations

A better understanding of the distribution of the microbialites, which act as important substrates for other elements in the lake's food chain, will assist in managing and protecting the GSL ecosystem. In a wider context, GSL is part of the world avian ecosystem and a vital component of the Western Hemisphere Shorebird Reserve Network (Baxter, 2018; Baxter & Butler, 2020). The lake and its marshes provide a resting and staging area for between 2 and 5 million shorebirds, as many as 1.7 million eared grebes, and hundreds of thousands of waterfowl during spring and fall migration; the birds rely on the GSL area as a feeding ground as they migrate.

Microbial bioherms play a critical role in the primary production in the GSL ecosystem (Baxter & Butler, 2020; Lindsay et al., 2019, 2020; Marden et al., 2020), yet detailed information about the extent and function of the microbial mat-dominated benthos has heretofore not been widely available. Until the start of this investigation, the contributions of the sublittoral microbial communities that populate the benthos in GSL were very sparsely documented. Microbial bioherms and similar biogenic carbonates form the stable base for adherence of benthic biological forms such as brine fly larvae and the base for critical primary production during periods of water-column overgrazing by brine shrimp. Baseline information about the occurrence, distribution, morphology, biology and development of microbial structures is critical in understanding the role of this benthic community on the ecology and health of GSL, the long-term hydrologic history of the lake, and the effects of anthropogenic influences on the environment of the lake. Knowing the extent and location of the microbial bioherms allows researchers and managers to estimate primary productivity and food availability for avian populations. Changes in climate, increases in water diversions for human use and the introduction of waste materials from human activities adjacent to the lake threaten the stability of the lake and the organisms depending on it for their survival.

There is an extensive literature on microbialites in non-marine settings, in modern and ancient lakes (cf. Alonzo-Zarza et al., 2020; Arp et al., 1999a, 1999b; Burne & Moore, 1987; Burne et al., 2014; Della Porta, 2015; Gierlowski-Kordesch, 2010; Kempe et al., 1991; Riding, 2000; Sarg et al., 2013; Wright, 2012; and references therein), but the scale of the distribution of those in GSL provides a unique opportunity to assess their key controls. Salinity as stated above is a critical control with the extreme salinity of the north arm preventing benthic microbial mat growth and hence microbialites, and probably also in relation to the halocline. Sedimentation is another critical factor where even localised variations associated with small-scale fault-related elevation differences have had a profound effect on microbialite growth. Sediment disturbance is a key control on microbialite growth rates and spatial distribution in ancient marine (Curtis et al., 2021; Johnson & Grotzinger, 2006) and lacustrine (Andrews & Trewin, 2014) microbial carbonates.

6 | CONCLUSIONS

The GSL provides a unique and ideal scenario for studying environmental and anthropogenic controls on the occurrence and distribution of microbial bioherms within a mid-latitude shallow lacustrine environment. The identification of factors that influence microbial bioherm occurrence and spatial distribution in GSL is limited to a set of collinear physical, chemical and biological variables that are confined to a localised closed system. Recent investigations of GSL microbial bioherms have focused on easily accessible bioherms exposed in the littoral zone and from nearshore sublittoral areas as water clarity, access limitations, logistical issues, and the difficulties of sampling in high-salinity waters have prevented studies of the deeper parts of the lake. This study resolved the difficulties of sampling in the deeper waters of GSL and focused on microbial bioherm occurrence and distribution in the sublittoral zone, which will provide a basis for further studies.

The reprocessing of acoustic data from earlier bathymetric surveys, verified with additional side-scan sonar and CHIRP mapping and diving, video and sampling and laboratory analyses have enabled the distribution of sublittoral microbial bioherms to be assessed. Bioherms occupy an estimated area of more than 700 km^2 in the south arm of GSL and more than 300 km^2 along the margins of the north arm. Salinity, water depth, sedimentation and substrate condition all affect bioherm distributions, which vary from statistically dispersed to clustered. For the latter case concentrations are located on metre-scale, fault-controlled topographic highs, with sediment infilling intervening lows and onlapping the hanging-wall slopes. Thus, subtle changes in depth and sedimentation resulting from recent tectonic deformation directly affect microbial bioherm occurrence and spatial distribution throughout the lake. The abrupt occurrence of bioherms in areas of small positive topographic relief indicates an acute sensitivity to environmental gradients. Based on the observed relationship between metre-scale tectonic features and pervasive bioherm distributions along the shallow margins of the lake, it appears that depth-related factors such as light availability and/or wave and current energy and detrital sediment input to the microbial mats, play a role in bioherm distribution.

Individual sublittoral bioherms typically are circular to oblate, and range in size from centimetres to over 2 m in diameter, locally with heights above the substrate of more than 1.5 m. In terms of morphology, the bioherms are dominated by domal and columnar forms, with no significant mineralogical, textural or stable carbon and oxygen isotope signature differences when compared to shoreline bioherms. Carbonate precipitated fabrics consist of clotted peloidal micrite-grade and fibrous spherulitic boundstone associated with microbial biofilm EPS as observed in other lacustrine and marine microbialites in the recent and geological record.

Due to anthropogenic factors, in this case the construction of a rock-filled causeway that divided GSL in 1959, salinity increases in the north arm have exceeded a threshold for viability of bioherm-mediating microbial mat communities and microbialite formation has been terminated. In addition to providing valuable information for studying the effects of the benthic microbial community on the ecology and health of GSL, the study of microbial bioherm distributions in GSL may also provide insights into the physical and chemical controls that existed during the formation of fossil lacustrine and marine microbialites in the geological record.

ACKNOWLEDGEMENTS

CONFLICT OF INTEREST

The authors declare no conflict of interest.

DATA AVAILABILITY STATEMENT

The authors confirm that the data supporting the findings of this study are available within the article and its supporting information files; additional data are available from the corresponding author upon request.

ORCID

Giovanna Della Porta https://orcid.org/0000-0003-3479-0592
V. Paul Wright https://orcid.org/0000-0003-1251-8432

REFERENCES

Almeida-Dalmet, S., Litchfield, C.D., Gillevet, P. & Baxter, B.K. (2018) Differential gene expression in response to salinity and temperature in a *Haloarcula* Strain from Great Salt Lake, Utah. *Genes*, 9, 52. https://doi.org/10.3390/genes9010052

Almeida-Dalmet, S., Sikaroodi, M., Gillevet, P., Litchfield, C.D. & Baxter, B.K. (2015) Temporal study of the microbial diversity of the north arm of Great Salt Lake, Utah, U.S. *Microorganisms*, 3, 310–326.

Alonso-Zarza, A.M., Cabaleri, N.G., Huerta, P., Armella, C., Rodríguez-Berriguete, Á., Monferran, M.D., Gallego, O.F., Ubaldon, M.C. & Nieto, D.S. (2020) Lacustrine microbialite pinnacles in the Palaeogene of Patagonia, Argentina: facies and controls. *Sedimentary Geology*, 408, 105742.

Andrews, S.D. & Trewin, N.H. (2014) Palaeoenvironmental significance of lacustrine stromatolite forms from the Middle Old Red Sandstone of the Orcadian Basin. *Geological Magazine*, 151, 414–429.

Armstrong, P.A., Taylor, A.R. & Ehlers, T.A. (2004) Is the Wasatch fault footwall (Utah, United States) segmented over million-year time scales? *Geology*, 32, 385–388. https://doi.org/10.1130/G20421.1

Arnow, T. (1984) Water-level and water-quality changes in Great Salt Lake Utah, 1847-1983. U.S. Geological Survey Circular 913, 22 pp. https://pubs.usgs.gov/circ/1984/0913/report.pdf

Arnow, T. & Stephens, D. (1990) Hydrologic characteristics of the Great Salt Lake, Utah: 1847-1986. U.S. Geological Survey Water-supply Paper 2332, 32 p.

Arp, G., Reimer, A. & Reitner, J. (1999a) Calcification in cyanobacterial biofilms of alkaline salt lakes. *European Journal of Phycology*, *34*, 393–403.

Arp, G., Reimer, A. & Reitner, J. (2001) Photosynthesis-induced biofilm calcification and calcium concentrations in Phanerozoic oceans. *Science*, *292*, 1701–1704.

Arp, G., Reimer, A. & Reitner, J. (2002) Calcification of cyanobacterial filaments: *Girvanella* and the origin of lower Paleozoic lime mud. Comment and Reply: comment. *Geology*, *30*, 579–580.

Arp, G., Reimer, A. & Reitner, J. (2003) Microbialite formation in seawater of increased alkalinity, Satonda Crater Lake, Indonesia. *Journal of Sedimentary Research*, *73*, 105–127.

Arp, G., Thiel, V., Reimer, A., Michaelis, W. & Reitner, J. (1999b) Biofilm exopolymers control microbialite formation at thermal springs discharging into the alkaline Pyramid Lake, Nevada, USA. *Sedimentary Geology*, *126*, 159–176.

Baskin, R.L. (2005) Calculation of area and volume for the south part of Great Salt Lake, Utah. U.S. Geological Survey Open-File Report 2005-1327, 6 p. http://pubs.er.usgs.gov/publication/ofr20051327

Baskin, R.L. (2006) Calculation of area and volume for the north part of Great Salt Lake, Utah. U.S. Geological Survey Open-File Report 2006-1359, 6 pp. http://pubs.er.usgs.gov/publication/ofr20061359

Baskin, R.L. (2014) Occurrence and spatial distribution of microbial bioherms in Great Salt Lake, Utah. Doctoral Dissertation, University of Utah.

Baumgartner, L.K., Reid, R.P., Dupraz, C., Decho, A.W., Buckley, D.H., Spear, J.R., Przekop, K.M. & Visscher, P.T. (2006) Sulfate reducing bacteria in microbial mats: changing paradigms, new discoveries. *Sedimentary Geology*, *185*, 131–145.

Baxter, B.K. (2018) Great Salt Lake microbiology: a historical perspective. *International Microbiology*, *21*, 79–95.

Baxter, B.K., Butler, J.K. (Eds.) (2020) *Great Salt Lake Biology – a terminal lake in a time of change*. Switzerland AG: Springer Nature, 527 pp. https://doi.org/10.1007/978-3-030-40352-2_1

Belovsky, G.E., Stephens, D., Perschon, C., Birdsey, P., Paul, D., Naftz, D., Baskin, R., Larson, C., Mellison, C., Luft, J., Mosley, R., Mahon, H., Van Leeuwen, J. & Allen, D.V. (2011) The Great Salt Lake Ecosystem (Utah, USA): long term data and a structural equation approach. *Ecosphere*, *2*, 1–40.

Benzerara, K., Meibom, A., Gautier, Q., Kazmierczak, J., Stolarski, J., Menguy, N. & Brown, G.E. Jr. (2010) Nanotextures of aragonite in stromatolites from the quasi-marine Satonda crater lake, Indonesia. In: Pedley, H.M. & Rogerson, M. (Eds.) *Tufas and speleothems: unravelling the microbial and physical controls*. *Geological Society London, Special Publications*, *336*, 211–224.

Bontognali, T.R., Vasconcelos, C., Warthmann, R.J., Bernasconi, S.M., Dupraz, C., Strohmenger, C.J. & Mckenzie, J.A. (2010) Dolomite formation within microbial mats in the coastal sabkha of Abu Dhabi (United Arab Emirates). *Sedimentology*, *57*, 824–844.

Bouton, A., Vennin, E., Amiotte-Suchet, P., Thomazo, C., Sizun, J.-P., Virgone, A., Gaucher, E.C. & Visscher, P.T. (2020) Prediction of the calcium carbonate budget in a sedimentary basin: a "source-to-sink" approach applied to Great Salt Lake, Utah, USA. *Basin Research*, *32*, 1005–1034.

Bouton, A.Vennin E., Boulle, J., Pace, A., Bourillot, R., Thomazo, C., Brayard, A., Désaubliaux, G., Goslar, T., Yokoyama, Y. & Dupraz, C. (2016a) Linking the distribution of microbial deposits from the Great Salt Lake (Utah, USA) to tectonic and climatic processes. *Biogeosciences*, *13*(19), 5511–5526.

Bouton, A., Vennin, E., Mulder, T., Pace, A., Bourillot, R., Thomazo, C., Brayard, A., Goslar, T., Buoncristiani, J.F., Désaubliaux, G. & Visscher, P.T. (2016b) Enhanced development of lacustrine microbialites on gravity flow deposits, Great Salt Lake, Utah, USA. *Sedimentary Geology*, *341*, 1–12.

Burne, R.V. & Moore, L.S. (1987) Microbialites: organosedimentary deposits of benthic microbial communities. *Palaios*, *2*, 241–254.

Burne, R.V., Moore, L.S., Christy, A.G., Troitzsch, U., King, P.L., Carnerup, A.M. & Hamilton, P.J. (2014) Stevensite in the modern thrombolites of Lake Clifton Western Australia: a missing link in microbial mineralization? *Geology*, *42*, 575–578.

Carozzi, A.V. (1962) Observations on algal biostromes in the Great Salt Lake, Utah. *Journal of Geology*, *70*, 246–252.

Chidsey, T.C. Jr, Vanden Berg, M.D. & Eby, D.E. (2015) Petrography and characterization of microbial carbonates and associated facies from modern Great Salt Lake and Uinta Basin's Eocene Green River Formation in Utah, USA. In: Bosence, D.W.J., Gibbons, K.A., Le Heron, D.P., Morgan, W.A., Pritchard, T. & Vining, B.A. (Eds.) *Microbial carbonates in space and time: implications for global exploration and production. Geological Society London Special Publication*, *418*, 261–286.

Colman, S.M., Kelts, K.R. & Dinter, D.A. (2002) Depositional history and neotectonics in Great Salt Lake, Utah, from high-resolution seismic stratigraphy. *Sedimentary Geology*, *148*, 61–78.

Corsetti, F.A., Anderson, R.P., Bird, J., Meneske, M., Stefurak, E., Petryshyn, V.A., Tripati, A., Stamps, B.W., Stevenson, B.S. & Spear, J.R. (2013) Ooid formation in the Great Salt Lake, Utah – insights from clumped isotope paleothermometry and molecular biology. Abstract – Geological Society of America, Denver, CO.

Curtis, A., Wood, R., Bowyer, F., Shore, A., Curtis-Walcott, A. & Robertsson, J. (2021) Modelling Ediacaran metazoan–microbial reef growth. *Sedimentology*, https://doi.org/10.1111/sed.12832

Della Porta, G. (2015) Carbonate build-ups in lacustrine, hydrothermal and fluvial settings: comparing depositional geometry, fabric types and geochemical signature. In: Bosence, D.W.J., Gibbons, K.A., Le Heron, D.P., Morgan, W.A., Pritchard, T. & Vining, B.A. (Eds.), *Microbial carbonates in space and time: implications for global exploration and production. Geological Society of London Special Publications*, *418*, 17–68.

Diaz, X., Johnson, W.P., Fernandez, D. & Naftz, D.L. (2009) Size and elemental distributions of nano to micro-particulates in the geochemically-stratified Great Salt Lake. *Applied Geochemistry*, *24*, 1653–1665.

Dinter, D.A. & Pechmann, J.C. (1999) Multiple Holocene earthquakes on the East Great Salt Lake fault, Utah – evidence from high-resolution seismic reflection data. *EOS, Transactions of the American Geophysical Union*, *80*(46 Suppl.), F734.

Dinter, D.A. & Pechmann, J.C. (2014) Paleoseismology of the promontory segment. https://earthquake.usgs.gov/cfusion/external_grants/research.cfm

Dunham, E.C., Fones, E.M., Fang, Y., Lindsay, M.R., Steuer, C., Fox, N., Willis, M., Walsh, A., Colman, D.R., Baxter, B.K., Lageson, D., Mogk, D., Rupke, A., Xu, H. & Boyd, E.S. (2020) An ecological perspective on dolomite formation in Great Salt Lake, Utah. *Frontiers in Earth Sciences*, *8*, 24. https://doi.org/10.3389/feart.2020.00024

Dupraz, C.R., Reid, P., Braissant, O., Decho, A.W., Norman, R.S. & Visscher, P.T. (2009) Processes of carbonate precipitation in modern microbial mats. *Earth-Science Reviews*, *96*, 141–162.

Dupraz, C. & Visscher, P.T. (2005) Microbial lithification in marine stromatolites and hypersaline mats. *Trends in Microbiology*, *13*(9), 10.

Dupraz, C., Visscher, P.T., Baumgartner, L.K. & Reid, R.P. (2004) Microbe–mineral interactions: early carbonate precipitation in a hypersaline lake (Eleuthera Island, Bahamas). *Sedimentology*, *51*(4), 745–765.

Eardley, A.J. (1938) The sediments of Great Salt Lake, Utah. *Bulletin American Association of Petroleum Geologists*, *22*, 1305–1411.

Eardley, A.J., Gvosdetsky, V. & Marsell, R.E. (1957) Hydrology of Lake Bonneville and sediments and soils of its basin. *Geological Society American Bulletin*, *68*, 1141–1201.

Friedlander, A.M. & Parrish, J.D. (1998) Habitat characteristics affecting fish assemblages on a Hawaiian coral reef. *Journal of Experimental Marine Biology and Ecology*, *224*, 1–30.

Ge, Y., Della Porta, G., Pederson, C.L., Lokier, S.W., Hoffmann, R. & Immenhauser, A. (2021) Botryoidal and spherulitic aragonite in carbonates associated with microbial mats: precipitation or diagenetic replacement product? *Frontiers in Earth Sciences*, *9*, 698952. https://doi.org/10.3389/feart.2021.698952

Getis, A. & Ord, J.K. (1992) The analysis of spatial association by use of distance statistics. *Geographical Analysis*, *24*(3), 189–206.

Gierlowski-Kordesch, E.H. (2010) Lacustrine carbonates. In: Alonso-Zarza, A.M. & Tanner, L.H. (Eds.) *Carbonates in continental settings: facies, environments and processes. Developments in Sedimentology*, *61*, 1–101.

Gilbert, G.K. (1890) Lake Bonneville. U.S. Geological Survey Monograph 1, 438 pp. U.S. Government Printing Office, Washington, DC.

Grim, R.E., Kulbricki, G. & Carozzi, A.V. (1960) Clay mineralogy of the sediments of the Great Salt Lake, Utah. *Geological Society of America Bulletin*, *71*(4), 515–519.

Hahl, D.C. & Handy, A.H. (1969) Great Salt Lake, Utah: chemical and physical variations of the Brine, 1963-1966. Utah Geological and Mineralogical Survey Water Resources Bulletin, 12, 34 pp.

Hahl, D.C. & Langford, R.H. (1964) Dissolved-mineral inflow to Great Salt Lake and characteristics of the salt lake brine – part II, technical report. Utah Geological and Mineralogical Survey. *Water Resources Bulletin*, *3*, 40.

Halley, R.B. (1976) Textural variation within Great Salt Lake algal mounds. In: Walter, M.R. (Ed.) *Stromatolites: developments in sedimentology 20*. Amsterdam: Elsevier Scientific Publishing Company.

Halley, R.B. (1977) Ooid fabric and fracture in the Great Salt Lake and the geologic record. *Journal of Sedimentary Petrology*, *47*(3), 1099–1120.

Hedberg, L.L. & Parry, W.T. (1971) Clay mineralogy at the brine-sediment interface in the south arm of Great Salt Lake, Utah. Utah Geological and Mineralogical Survey, Special Studies 35.

Ingalls, M., Frantz, C.M., Snell, K.E. & Trower, E.J. (2020) Carbonate facies-specific stable isotope data record climate, hydrology, and microbial communities in Great Salt Lake, UT. *Geobiology*, *18*(5), 566–593.

Jaramillo-Vogel, D., Foubert, A., Braga, J.C., Schaegis, J.-C., Atnafu, B., Grobety, B. & Kidane, T. (2019) Pleistocene sea-floor fibrous crusts and spherulites in the Danakil Depression (Afar, Ethiopia). *Sedimentology*, *66*, 480–512.

Johnson, J. & Grotzinger, J.P. (2006) Effect of sedimentation on stromatolite reef growth and morphology, Ediacaran Omkyk Member (Nama Group), Namibia. *South African Journal of Geology*, *109*, 87–96.

Jones, B. (2017) Review of calcium carbonate polymorph precipitation in spring systems. *Sedimentary Geology*, *353*, 64–75.

Jones, B.F., Naftz, D.L., Spencer, R.J. & Oviatt, C.G. (2009) Geochemical evolution of Great Salt Lake, Utah, USA. *Aquatic Geochemistry*, *15*, 95–121.

Jones, B. & Peng, X. (2014) Signatures of biologically influenced $CaCO_3$ and Mg–Fe silicate precipitation in hot springs: case study from the Ruidian geothermal area, western Yunnan Province, China. *Sedimentology*, *61*, 56–89.

Jones, E.F. & Wurtsbaugh, W.A. (2014) The Great Salt Lake's monimolimnion and its importance for mercury bioaccumulation in brine shrimp (*Artemia franciscana*). *Limnology and Oceanography*, *59*, 141–155. 10.4319.lo.2014.59.01.0141

Kahle, C.F. (1974) Ooids from Great Salt Lake, Utah, as an analogue for the genesis and diagenesis of ooids in marine limestones. *Journal of Sedimentary Petrology*, *44*, 30–39.

Katzenburger, W.M. & Whelan, J.A. (1975) Currents of the Great Salt Lake, Utah. *Utah Geology*, *2*, 103–107.

Kempe, S., Kazmierczak, J., Landmann, G., Konuk, T., Reimer, A. & Lipp, A. (1991) Largest known microbialites discovered in Lake Van, Turkey. *Nature*, *349*(6310), 605–608.

Kjeldsen, K.U., Loy, A., Jakobsen, T.F., Thomsen, T.R., Wagner, M. & Ingvorsen, K. (2007) Diversity of sulfate-reducing bacteria from an extreme hypersaline sediment, Great Salt Lake (Utah). *FEMS Microbiology and Ecology*, *60*, 287–298.

Kowalewska, A. & Cohen, A.S. (1998) Reconstruction of paleoenvironments of the Great Salt Lake Basin during the late Cenozoic. *Journal of Paleolimnology*, *20*, 381–407.

Kremer, B., Kazmierczak, J. & Kempe, S. (2019) Authigenic replacement of cyanobacterially precipitated calcium carbonate by Al-silicates in giant microbialites of Lake Van (Turkey). *Sedimentology*, *66*, 285–304.

Lin, A. (1976) A survey of the physical limnology of the Great Salt Lake. Utah Division of Water Resources and University of Utah, 82 pp.

Lindsay, M.R., Anderson, C., Fox, N., Scofield, G., Allen, J., Anderson, E., Bueter, L., Poudel, S., Sutherland, K., Munson-McGee, J.H., Van Nostrand, J.D., Zhou, J., Spear, J.R., Baxter, B.K., Lageson, D.R. & Boyd, E.S. (2017) Microbialite response to an anthropogenic salinity gradient in Great Salt Lake, Utah. *Geobiology*, *15*, 131–145. https://doi.org/10.1007/978-3-030-40352-2_4

Lindsay, M.R., Dunham, E.C. & Boyd, E.S. (2020) Microbialites of Great Salt Lake. In: Baxter, B.K. & Butler, J.K. (Eds.) *Great Salt Lake biology – a terminal lake in a time of change*. Switzerland AG: Springer Nature, pp. 87–118. https://doi.org/10.1007/978-3-030-40352-2_4

Lindsay, M.R., Johnston, R.E., Baxter, B.K. & Boyd, E.S. (2019) Effects of salinity on microbialite-associated production in Great Salt Lake, Utah. *Ecology*, *100*(3), e02611. https://doi.org/10.1002/ecy.2611

Loving, B.L., Miller, C.W. & Waddell, K.M. (2000) Water and salt balance of Great Salt Lake, Utah, and simulation of water and salt movement through the Causeway, 1987-98. U.S. Geological Survey Water-Resources Investigations Report 00-4221. https://doi.org/10.3133/wri004221. https://pubs.er.usgs.gov/publication/wri004221

Madsen, D.B., Rhode, D., Grayson, D.K., Broughton, J.M., Livingston, S.D., Hunt, J., Quade, J., Schmitt, D.N. & Shaver, M.W. III (2001) Late Quaternary environmental change in the Bonneville basin, western USA. *Palaeogeography, Palaeoclimatology, Palaeoecology*, *167*, 243–271.

Malde, H.E. (1968) The catastrophic late Pleistocene Bonneville flood in the Snake River plain, Idaho. *U.S. Geological Survey Professional Paper*, *596*, 52 pp.

Marden, B., Brown, P. & Bosteels, T. (2020) Great Salt Lake Artemia: ecosystem functions and services with a global reach. In: Baxter, B.K. & Butler, J.K. (Eds.) *Great Salt Lake biology – a terminal lake in a time of change*. Switzerland AG: Springer Nature, pp. 175–237. https://doi.org/10.1007/978-3-030-40352-2_7

Martín-Pérez, A., La Iglesia, Á., Almendros, G., González-Pérez, J.A. & Alonso-Zarza, A.M. (2021) Precipitation of kerolite and sepiolite associated with Mg-rich carbonates in a cave environment. *Sedimentary Geology*, *411*, 105793.

Meldrum, F.C. & Cölfen, H. (2008) Controlling mineral morphologies and structures in biological and synthetic systems. *Chemical Reviews*, *108*, 4332–4432.

Mikulich, M.J. & Smith, R.B. (1974) Seismic-reflection and aeromagnetic surveys of the Great Salt Lake, Utah. *Geological Society of America Bulletin*, *85*, 991–1002.

Miller, D.E. (1980) *Great Salt Lake: a historical sketch. Utah Geological and Mineral Survey Bulletin 116: 1*. Salt Lake City, UT.

Mohapatra, G.K. & Johnson, R.A. (1998) Localization of listric faults a thrust fault ramps beneath the Great Salt Lake basin, Utah – evidence from seismic imaging and finite element modeling. *Journal of Geophysical Research*, *103*, 10047–10063.

Moran, P.A.P. (1950) Notes on continuous stochastic phenomena. *Biometrika*, *37*, 17–33.

Morrison, R.B. (1966) Predecessors of Great Salt Lake. In: Stokes, W.L. (Ed.) *The Great Salt Lake – guidebook to the geology of Utah*. Salt Lake City, UT: Utah Geological Society, pp. 77–104.

Moutoux, T.E. (1995) Palynological and tephra correlations among deep wells in the modern Great Salt Lake, Utah, USA – implications for a Neogene through Pleistocene climatic reconstruction. Unpublished M.Sc. thesis, Department of Geosciences, University of Arizona, Tucson, AZ.

Müller, G., Irion, G. & Forstner, U. (1972) Formation and diagenesis of inorganic Ca–Mg carbonates in the lacustrine environment. *Naturwissenschaften*, *59*, 158–164.

Murchison, S. (1989) *Fluctuation history of Great Salt Lake during the last 13,000 years*, PhD thesis. Salt Lake City, UT: University of Utah.

Newell, D.L., Jensen, J.L., Frantz, C.M. & Vanden Berg, M.D. (2017) Great Salt Lake (Utah) microbialite δ13C, δ18O, and δ15N record fluctuations in lake biogeochemistry since the late Pleistocene. *Geochemistry, Geophysics, Geosystems*, *18*, 3631–3645.

Nutz, A., Schuster, M., Ghienne, J.-f., Roquin, C. & Bouchette, F. (2018) Wind-driven waterbodies: a new category of lake within an alternative sedimentologically-based lake classification. *Journal of Paleolimnology*, *59*, 189–199. https://doi.org/10.1007/s10933-016-9894-2

O'Connor, J.E. (1993) Hydrology, hydraulics, and geomorphology of the Bonneville flood. *Geological Society of America, Special Paper*, *274*, 83.

Oviatt, C.G. (1997) Lake Bonneville fluctuations and global climate change. *Geology*, *25*, 155–158.

Oviatt, C.G. (2015) Chronology of Lake Bonneville, 30,000 to 10,000 yr B.P. *Quaternary Science Reviews*, *110*, 166–171.

Oviatt, C.G., Madsen, D.B., Miller, D.M., Thompson, R.S. & McGeehin, J.P. (2015) Early Holocene Great Salt Lake, USA. *Quaternary Research*, *84*(1), 57–68.

Pace, A., Bourillot, R., Bouton, A., Vennin, E., Galaup, S., Bundeleva, I., Patrier, P., Dupraz, C., Thomazo, C., Sansjofre, P., Yokoyama, Y., Franceschi, M., Anguy, Y., Pigot, L., Virgone, A. & Visscher, P.T. (2016) Microbial and diagenetic steps leading to the mineralisation of Great Salt Lake. *Scientific Reports*, *6*, 31495.

Pedley, M. (2014) The morphology and function of thrombolitic calcite precipitating biofilms: a universal model derived from freshwater mesocosm experiments. *Sedimentology*, *61*, 22–40.

Pedley, M., Rogerson, M. & Middleton, R. (2009) Freshwater calcite precipitates from in vitro mesocosm flume experiments: a case for biomediation of tufas. *Sedimentology*, *56*, 511–527.

Pedone, V.A. & Dickson, J.A.D. (2000) Replacement of aragonite by quasi-rhombohedral dolomite in a Late Pleistocene tufa mound, Great Salt Lake, Utah, USA. *Journal of Sedimentary Research*, *70*, 1152–1159.

Pedone, V.A. & Folk, R.L. (1996) Formation of aragonite cement by nannobacteria in the Great Salt Lake, Utah. *Geology*, *24*, 763–765.

Pedone, V.A. & Norgauer, C.H. (2002) Petrology and geochemistry of recent ooids from the Great Salt Lake, Utah. In: Gwynn, J.W. (Ed.), *Great Salt Lake – an overview of change*. Special publication of the Utah Department of Natural Resources, Utah Geological Survey. Salt Lake City, UT, pp. 33–41.

Perri, E., Tucker, M.E., Słowakiewicz, M., Whitaker, F., Bowen, L. & Perrotta, I.D. (2018) Carbonate and silicate biomineralization in a hypersaline microbial mat (Mesaieed sabkha, Qatar): roles of bacteria, extracellular polymeric substances and viruses. *Sedimentology*, *65*, 1213–1245.

Perri, E., Tucker, M.E. & Spadafora, A. (2012) Carbonate organo-mineral micro-and ultrastructures in sub-fossil stromatolites: Marion Lake, South Australia. *Geobiology*, *10*, 105–117.

Post, F.J. (1977) The microbial ecology of the Great Salt Lake. *Microbial Ecology*, *3*, 143–165.

Rawley, E.V. (1974) The Great Salt Lake biotic system. State of Utah, Department of Natural Resources, Division of Wildlife Resources publication 74-13, 431.

Reitner, J., Arp, G., Thiel, V., Gautret, P., Galling, U. & Michaelis, W. (1997) Organic matter in Great Salt Lake ooids (Utah, USA) – first approach to a formation of organic matrices. *Facies*, *36*, 210–219.

Rich, J. (2002) Great Salt Lake south arm circulation: currents, velocities and influencing factors. In: Gwynn, W. (Ed.) *Great Salt Lake – an overview of change*. Special Publication of the Utah Department of Natural Resources, Utah Geological Survey, pp. 171–183.

Riding, R. (2000) Microbial carbonates: the geological record of calcified bacterial-algal mats and biofilms. *Sedimentology*, *47*, 179–214.

Sandberg, P.A. (1975) New interpretations of Great Salt Lake ooids and of ancient non-skeletal carbonate mineralogy. *Sedimentology*, *22*, 497–537.

Sarg, J.F., Suriamin, N., TÌnavsuu-Milkeviciene, K. & Humphrey, J.D. (2013) Lithofacies, stable isotopic composition, and stratigraphic evolution of microbial and associated carbonates, Green River Formation (Eocene), Piceance Basin, Colorado. *AAPG Bulletin*, *97*, 1937–1966.

Spall, R. (2008) Basin-Scale Internal Waves within the South Arm of the Great Salt Lake. *International Journal of Modelling and Simulation*, *31*, 25–31. https://doi.org/10.1115/FEDSM2008-55084

Spencer, R.J., Baedecker, M.J., Eugster, H.P., Forester, R.M., Goldhaber, M.B., Jones, B.F., Kelts, K., McKenzie, J., Madsen, D.B., Rettig,

S.L., Rubin, M. & Bowser, C.J. (1984) Great Salt Lake, and precursors, Utah – the last 30,000 years. *Contributions to Mineralogy and Petrology*, *86*(4), 321–334.

Stephens, D.W. (1974) Limnological considerations of the Great Salt Lake, Utah. University of Utah Department of Biology Dissertation, 123 pp.

Stephens, D.W. (1990) Changes in lake levels, salinity and the biological community of Great Salt Lake (Utah, USA), 1847–1987. *Hydrobiologia*, *197*, 139–146.

Stephens, D.W. (1998) Salinity-induced changes in the aquatic ecosystem of Great Salt Lake, Utah. In: Pitman, J.K. & Carroll, A.R. (Eds) *Modern and ancient lake systems*. Utah Geological Association Guidebook 26. Salt Lake City, UT: Utah Geological Association, pp. 1–8.

Trower, E.J., Bridgers, S.L., Lamb, M.P. & Fischer, W.W. (2020) Ooid cortical stratigraphy reveals common histories of individual co-occurring sedimentary grains. *Journal of Geophysical Research: Earth Surface*, *125*(7), e2019JF005452.

Utah Department of Natural Resources (1997) Utah State water plan—Jordan River basin. Division of Water Resources, Salt Lake City, Utah.

Vanden Berg, M.D. (2019) Domes, rings, ridges, and polygons: characteristics of microbialites from Utah's Great Salt Lake. *The Sedimentary Record*, *17*, 4–10.

Vennin, E., Bouton, A., Bourillot, R., Pace, A., Roche, A., Brayard, A., Thomazo, C., Virgone, A., Gaucher, E.C., Desaubliaux, G. & Visscher, P.T. (2019) The lacustrine microbial carbonate factory of the successive Lake Bonneville and Great Salt Lake, Utah, USA. *Sedimentology*, *66*, 165–204. https://doi.org/10.1111/sed.12499

Waddell, K.M. & Barton, J.D. (1978) Estimated inflow and evaporation for Great Salt Lake, Utah, 1931–76, with revised model for evaluating the effects of dikes on the water and salt balance of the lake. U.S. Geological Survey Open, File Report 79-258, 61 p.

Waddell, K.M. & Bolke, E.L. (1973) The effects of restricted circulation on the salt balance of Great Salt Lake, Utah. Utah Geological Survey Water Resources Bulletin, 18, 54 p.

Waddell, K.M. & Fields, F.K. (1977) Model for evaluating the effects of dikes on the water and salt balance of Great Salt Lake, Utah. *Utah Geological Survey Water Resources Bulletin*, *21*, 54.

Wold, S.R., Thomas, B.E. & Waddell, K.M. (1997) Water and salt balance of Great Salt Lake, Utah, and simulation of water and salt movement through the causeway. U.S. Geological Survey Water, Supply Paper 2450, 64 p.

Wright, V.P. (2012) Lacustrine carbonates in rift settings: the interaction of volcanic and microbial processes on carbonate deposition. In: Garland, J., Neilson, J.E., Laubach, S.E. & Whidden, K.J. (Eds.) *Advances in carbonate exploration and reservoir analysis*. *Geological Society London, Special Publications*, *370*, 39–47.

Wurtsbaugh, W.A., Gardberg, J. & Izdepski, C. (2011) Biostrome communities and mercury and selenium bioaccumulation in the Great Salt Lake (Utah, USA). *Science of the Total Environment*, *409*(20), 4425–4434.

Zeyen, N., Daval, D., Lopez-Garciac, P., Moreirac, D., Gaillardet, J. & Benzerara, K. (2017) Geochemical conditions allowing the formation of modern lacustrine microbialites. *Proceedings of the Earth and Planetary Sciences*, *17*, 380–383.

SUPPORTING INFORMATION

Additional supporting information may be found online in the Supporting Information section.

Characteristics and controls on the distribution of sublittoral microbial bioherms in

Great Salt Lake, Utah: implications for understanding microbialite development

Robert L. Baskin[1], Giovanna Della Porta[2] and V. Paul Wright[3]

[1] RLB Research Alliance, North Salt Lake, Utah 84054, USA

(E-mail: rlbaskin@gmail.com)

[2] Earth Sciences Department, University of Milan, Via Mangiagalli 34, Milan 20133,

Italy

(E-mail: giovanna.dellaporta@unimi.it). Orcid 0000-0003-3479-0592

[3] Natural Sciences, National Museum of Wales, Cardiff, CF10 3NP, UK

(E-mail: v.vpw@btopenworld.com)
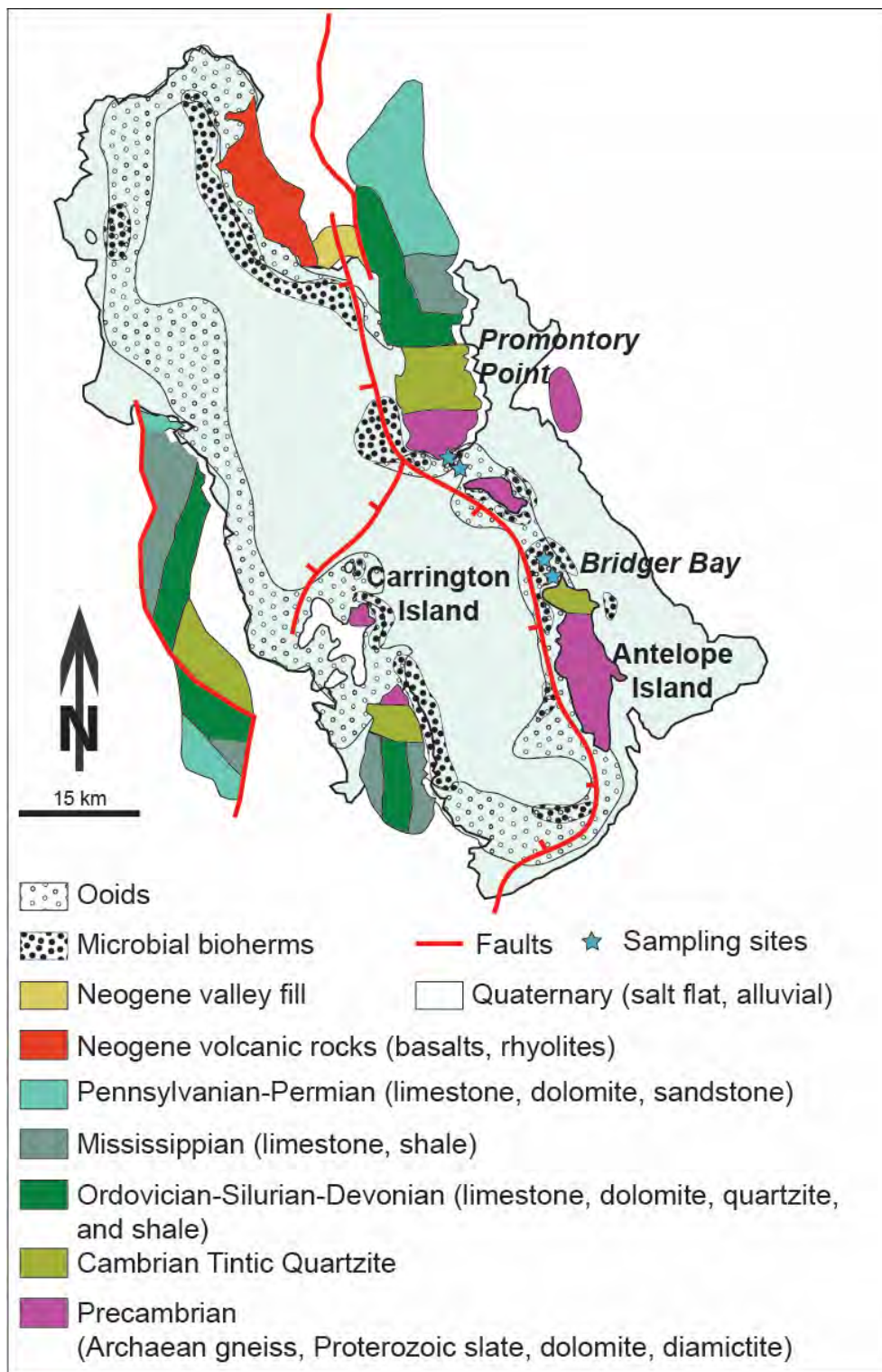
Figure S1. Schematic geological maps of Great Salt Lake (modified after Geological map of Utah produced by the Utah Geological Survey, http://geology.utah.gov/maps/geomap/index.htm) with faults extracted from Colman et al. (2002) and distribution of carbonate bioherms and ooids from Eardley (1938) and Carozzi (1962). Blue dots mark the location of sampling of the sublittoral bioherms at depths of 3-4 m.
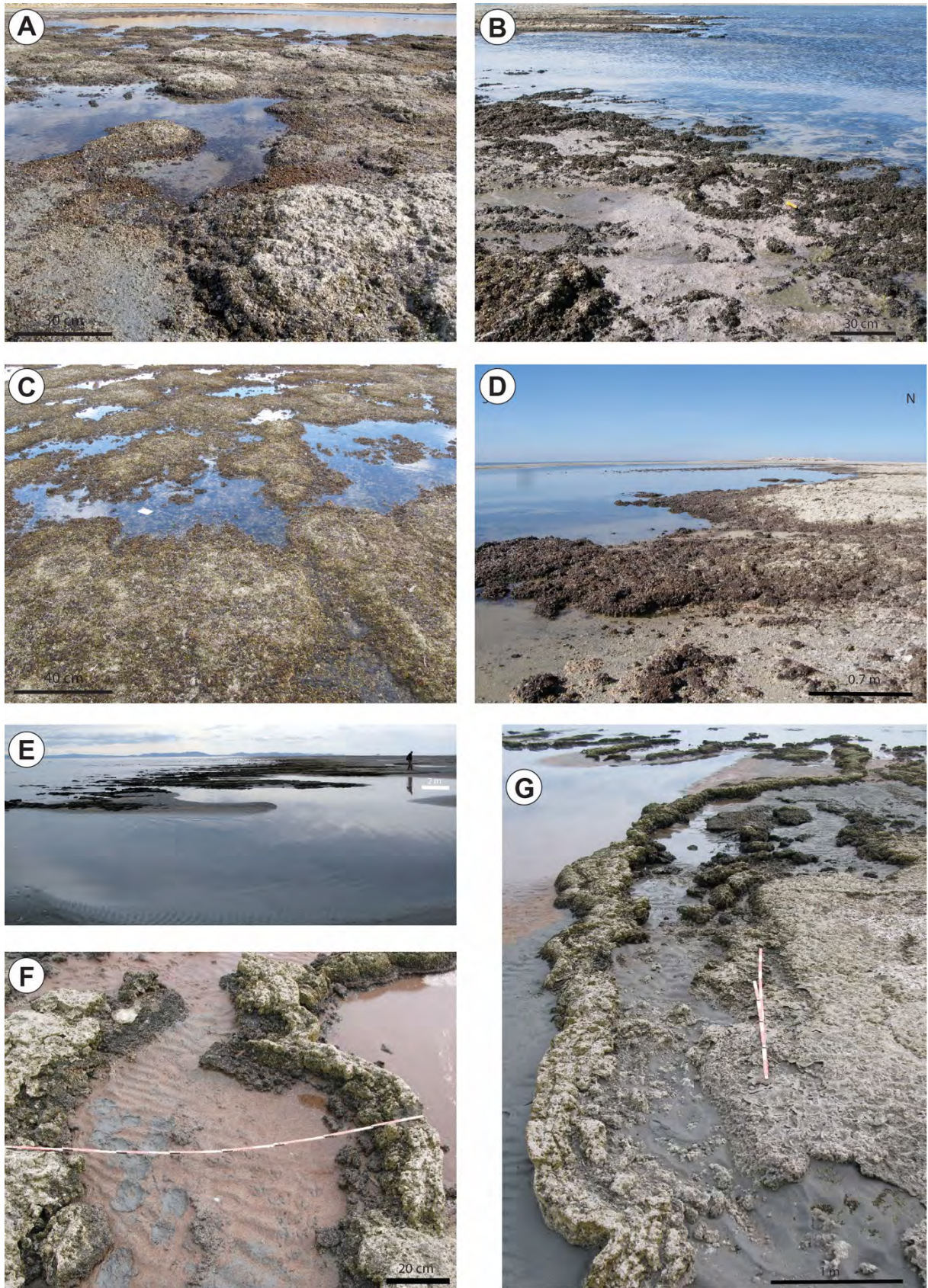
Figure S2. Photographs of exposed microbial bioherms at Bridger Bay (A-D) and Promontory Point (E-G).

Figure S3. Image showing recently exposed microbial bioherms along the south-west margin of the south arm of GSL that were excluded from the total estimate of occurrence due to shallow water conditions. Occurrences such as these are located within the vertical range of modern lake levels and are subject to periods of submergence and exposure, physical weathering and extreme temperature fluctuations. Large bioherm in foreground is *ca* 1 m in diameter at lake level. View is looking north-west along eastern edge of Stansbury Island. Image date is 2013 07 23. Lake surface elevation 1,278.8 m amsl.

Figure S4. Image showing exposed microbial bioherms along the south-west margin of the south arm of GSL. Water depth surrounding these bioherms was ca 0.8 m. Occurrences such as these are located within the vertical range of modern lake levels and are subject to periods of submergence and exposure, physical weathering and extreme temperature fluctuations. Bioherm in foreground is ca 0.6m in diameter. Image date is 2016 03 04. Lake surface elevation 1,278.2 m amsl.

Figure S5. Exposed microbial bioherms along the south-east margin of the north arm of GSL. Occurrences such as these are located within the vertical range of modern lake levels and are subject to periods of submergence and exposure, physical weathering and extreme temperature fluctuations. Bioherm in foreground is ca 1.5 m in diameter. Views are to south-west. Image date is 2011 01 30. Lake surface elevation 1,278.3 m amsl.

Figure S6. Recently exposed microbial bioherms along the south-west margin of the south arm of GSL. Water depth surrounding these bioherms was ca 0.4 m. Occurrences such as these are located within the vertical range of modern lake levels and are subject to periods of submergence and exposure, physical weathering and extreme temperature fluctuations. Bioherms in foreground are ca 1.2 m in diameter. View is looking west toward Stansbury Island. Image date is 2016 03 04. Lake surface elevation 1,278.2 m amsl.
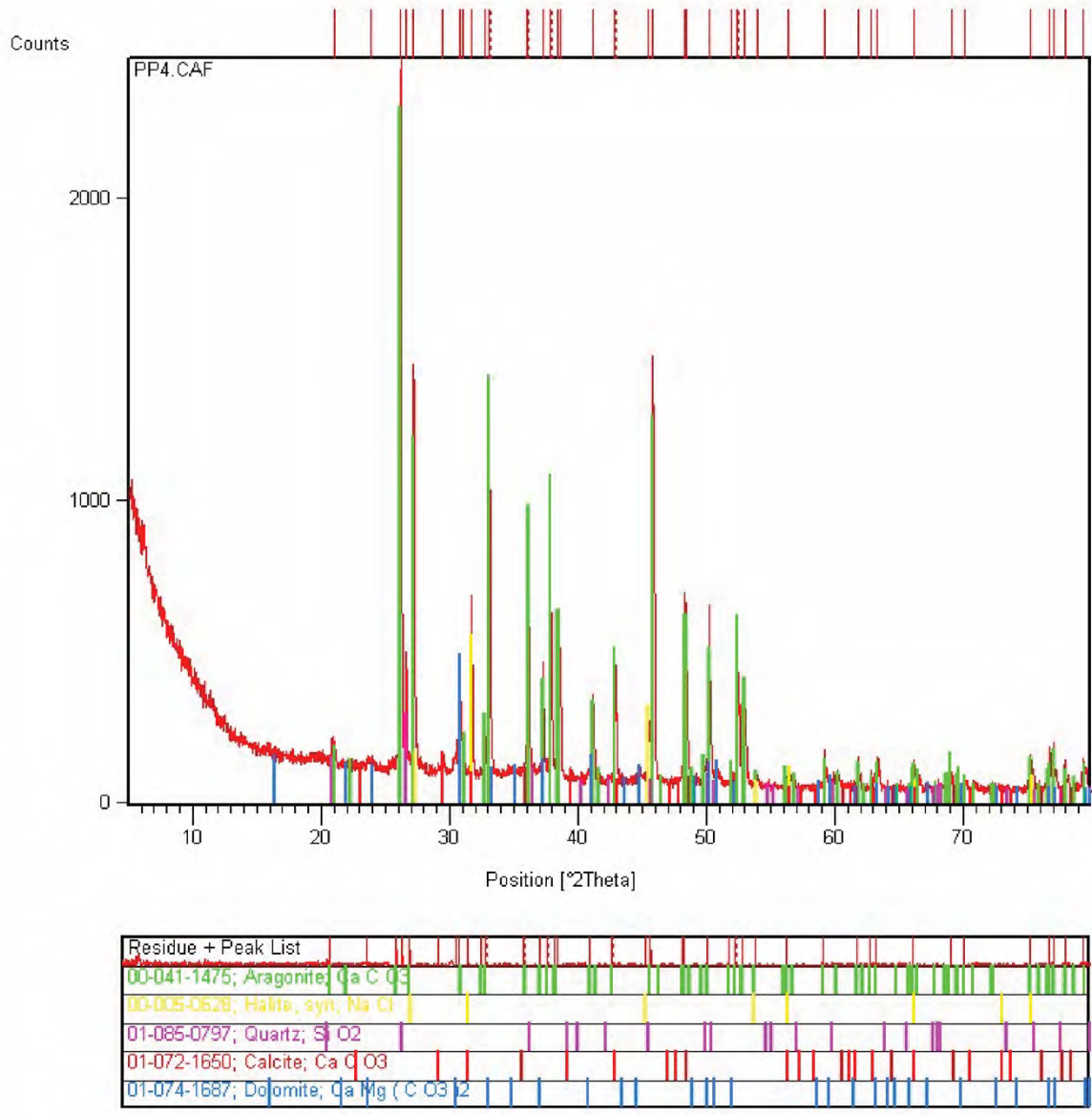
Figure S7. Results of XRD analyses of microbial bioherms at Promontory Point showing the predominance of aragonite associated with calcite, minor dolomite, halite and quartz.
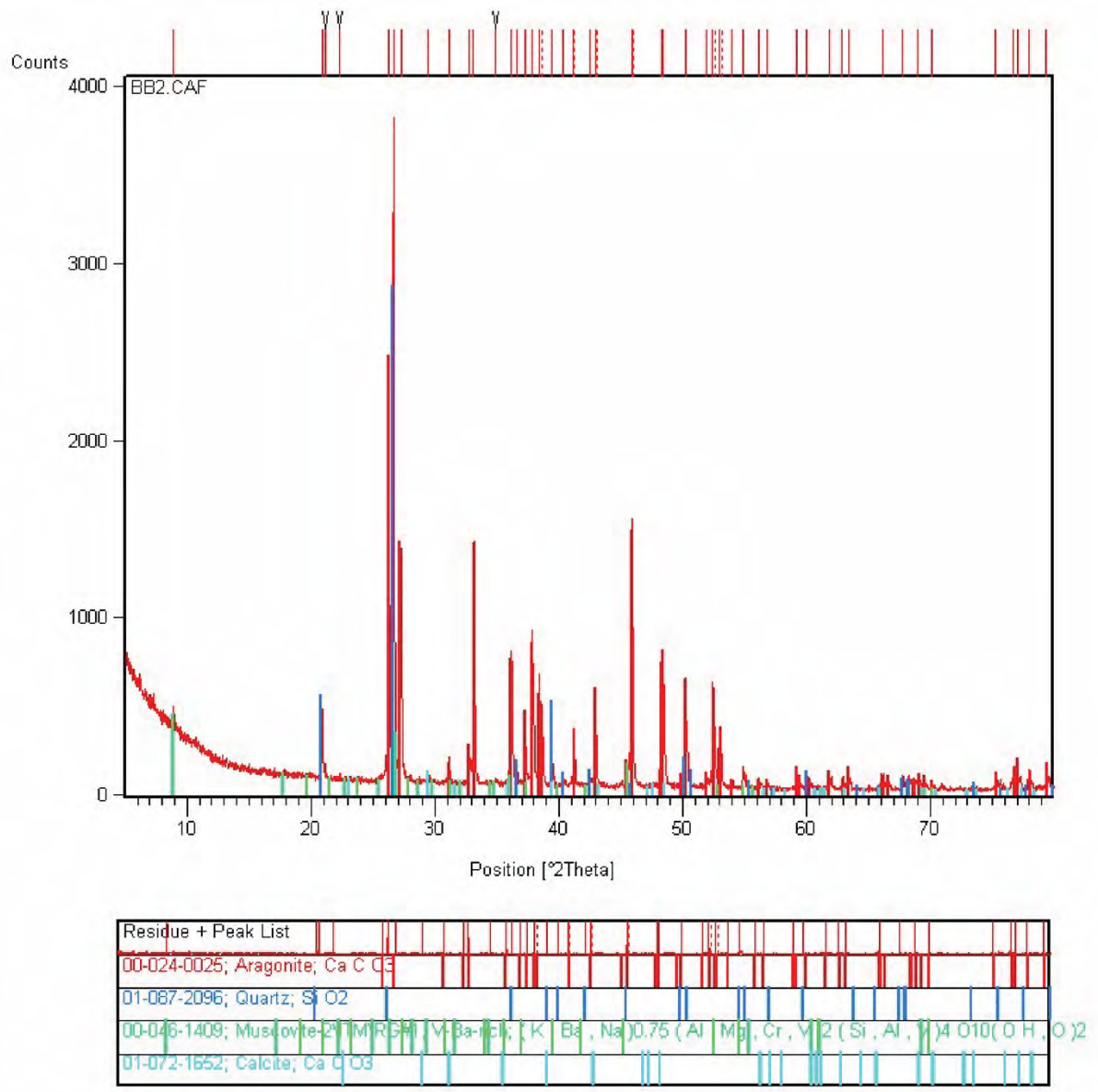
Figure S8. Results of XRD analyses of microbial bioherms at Bridger Bay showing the predominance of aragonite associated with calcite, quartz and a muscovite mica, probably of detrital origin.
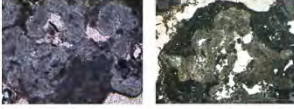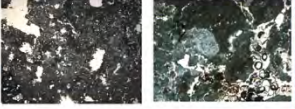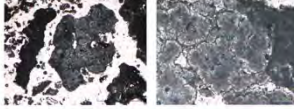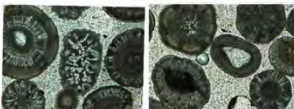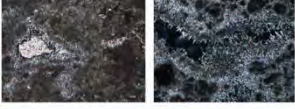
In situ precipitated boundstone and cementstone through biologically induced/influenced and physico-chemical processes				
	Precipitated fabric main components		**Primary Porosity**	**Secondary Porosity**
	Micrite Clotted peloidal micrite Microsparite	Microsparite (10-62 μm) Sparite Crystals (> 62 μm)		
Irregular framework	Clotted peloidal micrite/microsparite boundstone.	Sinuous threads of fibrous spherulitic microsparite/sparite boundstone lined by micrite crusts and aragonitic fibrous cement.	Framework connected Microporosity	Mouldic
Laminated	Laminated micrite boundstone overlying clotted peloidal and spherulitic microsparite boundstone.		Inter-laminae	
Components	**Grainy facies** Wackestone/Packstone	Grainstone	Primary Porosity	Secondary Porosity
Irregular spherulitic aggregate grains and bioherm-derived intraclasts		Grainstone of cm to mm size spherulitic grains and intraclasts of microbial bioherms	Interparticle, intraparticle, microporosity	Mouldic
Peloids, Ooids	Sparse peloids and ooids trapped within the clotted peloidal and spherulitic boundstone. Also in the cm- to dm- thick coatings on boulders .	Ooid grainstone in high energy shorelines	Interparticle, key-stone vugs	Moldic. Observed only on older boulder coatings.
Diagenetic Features	Early Cementation: early lacustrine aragonite needle cement. Halite precipitation .	Meteoric cementation: pendant to isopachous micritic to bladed calcite cement from vadose to phreatic meteoric cementing ooids in beachrocks.	Neomorphism: micrite recrystallization probably related to meteoric water in cm- to dm- thick coatings on boulders. Ooid fibers overgrowth.	Meteoric dissolution in cm- to dm- thick coatings on boulders.

Figure S9. Summary table of carbonate fabrics observed in GSL microbial bioherms, aggregate grains, ooids and older centimetre-thick carbonate crusts coating boulders on the shoreline of Promontory Point. The table summarises also the porosity types and diagenetic features.
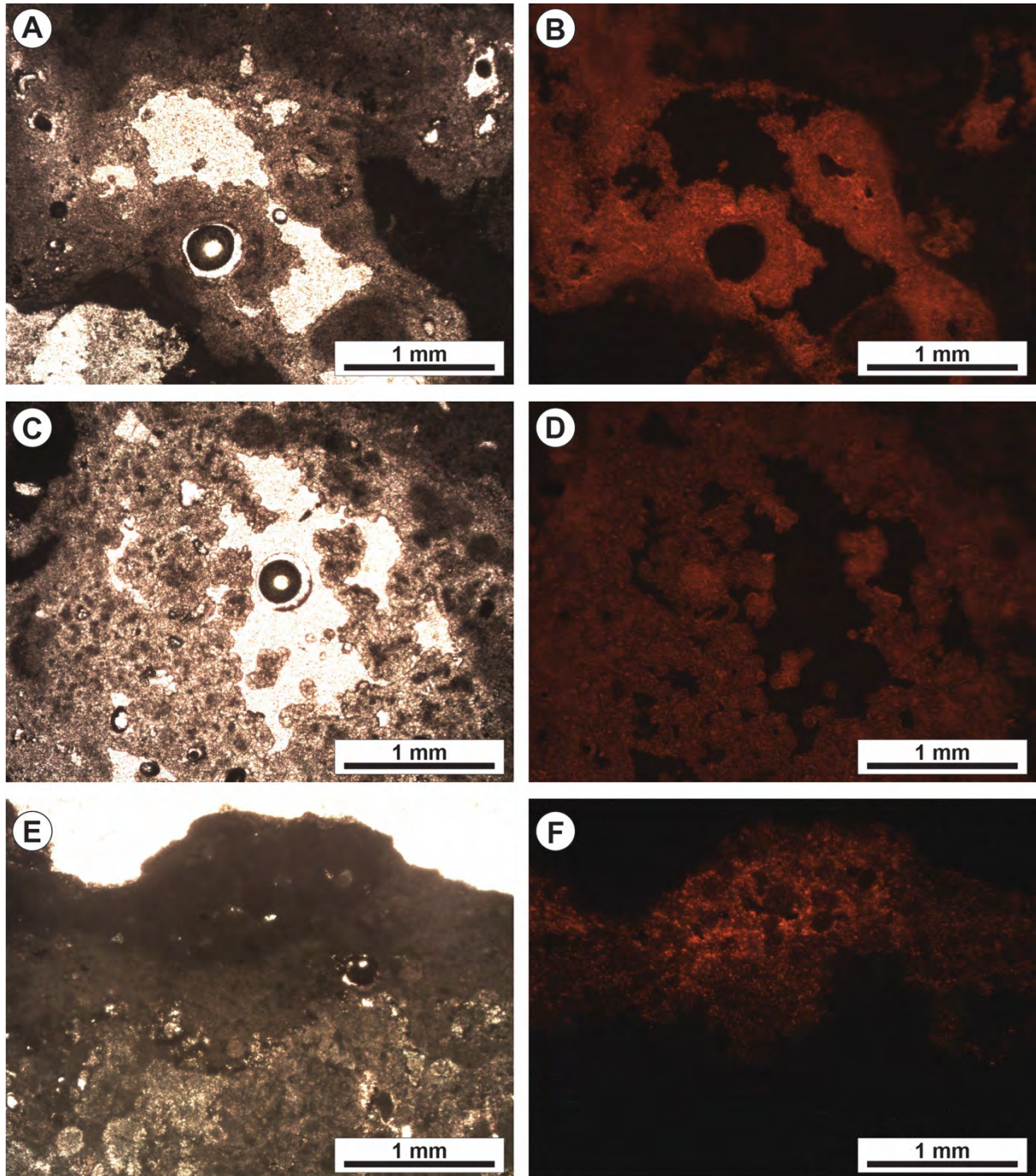
Figure S10. Cathodoluminescence analysis of microbial bioherms. A, C, E) Images in polarized light microscope. B, D, F) Images under cathodoluminescence showing that part of the clotted peloidal micrite-grade and spherulitic fabrics of the microbial bioherms are bright luminescent probably due to the presence of organic matter.
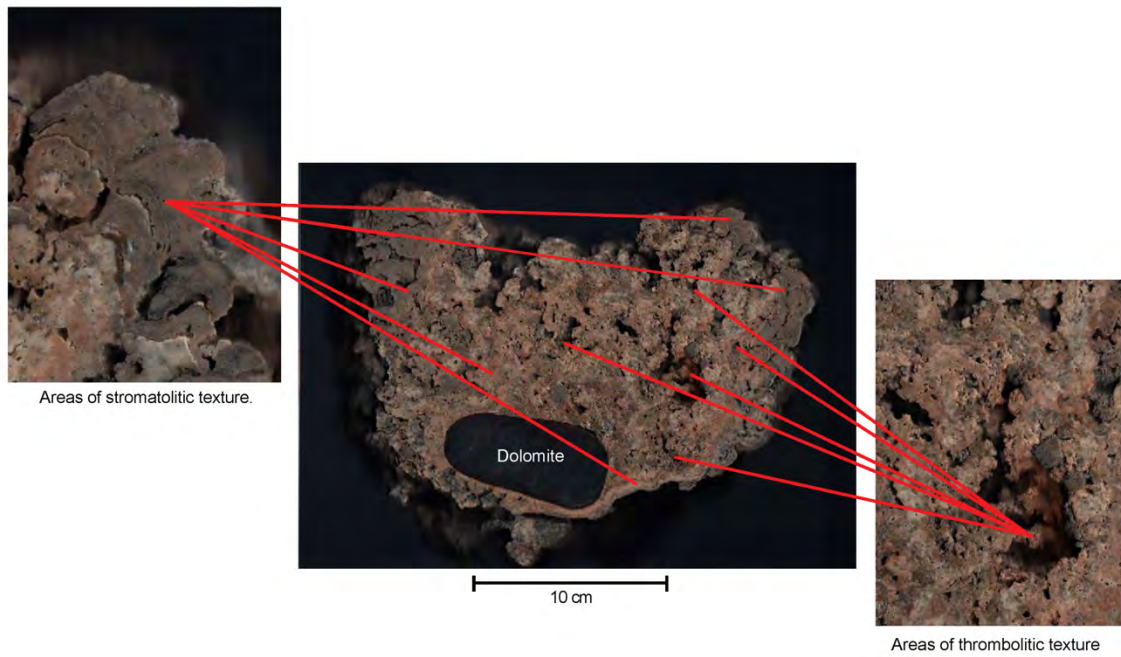
Areas of stromatolitic texture.

Dolomite

10 cm

Areas of thrombolitic texture

Figure S11. Cross-section of hand specimen of GSL microbial bioherm showing both laminated and clotted peloidal boundstone textures. Surveyed bioherms range in size from sub-decimetre through 2 m in width and over 1.5 m in height above surrounding sediments.
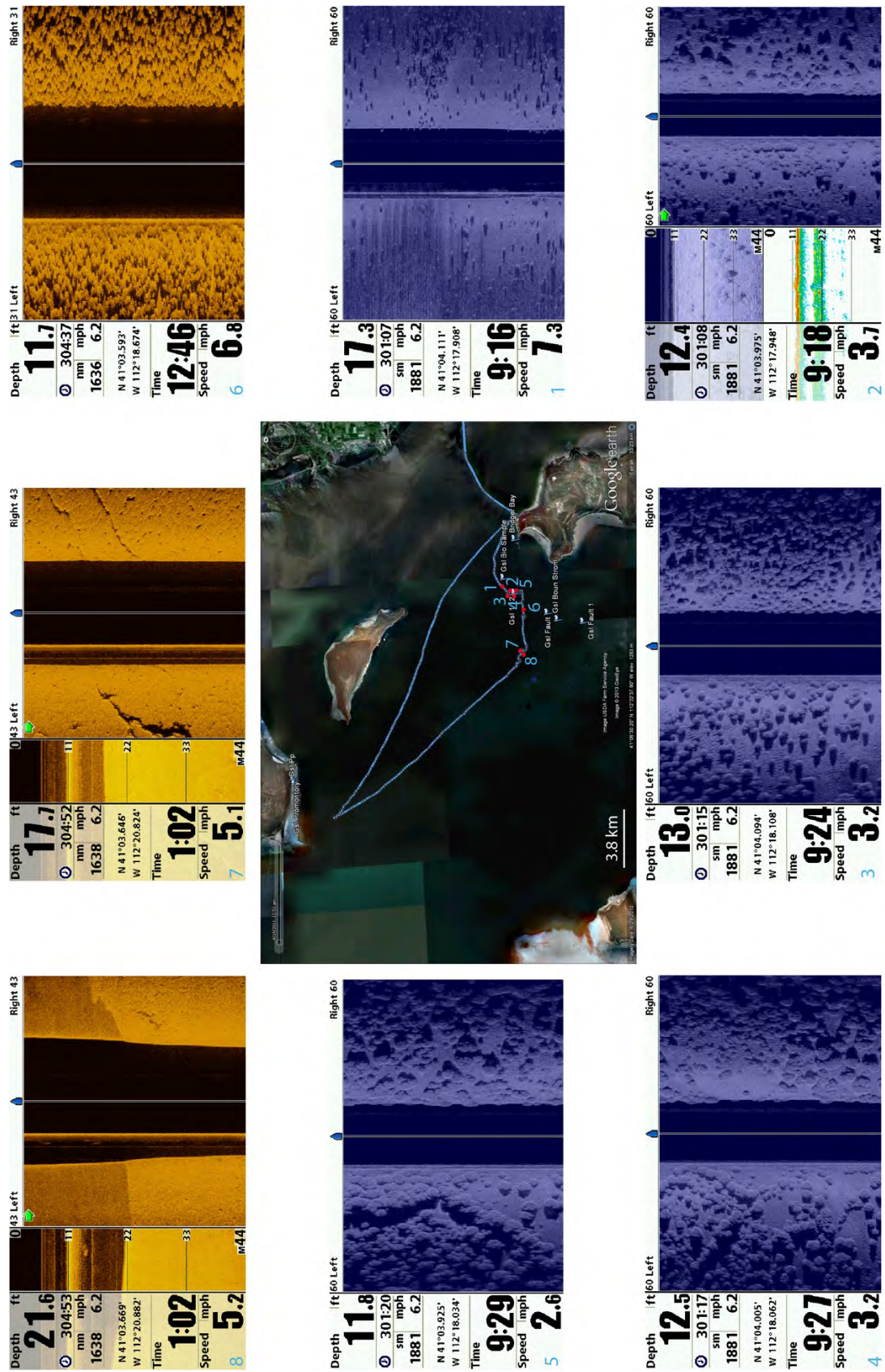
Figure S12. Satellite image from Google Earth showing the south arm portion between Bridger Bay and Promontory Point with location of the sampling site and side scan sonar images showing the distribution of sublittoral microbial bioherms.

Figure S13. Side scan sonar imagery showing pavement of continuous intergrowth microbial bioherm distribution grading to more dispersed distributions in deeper water east/north-east of Hat Island, south arm of GSL. Change in depth is from nearly 2.2 m to ca 3.5 m. Image date is 2009 07 09. Lake surface elevation ~1,276 m amsl.
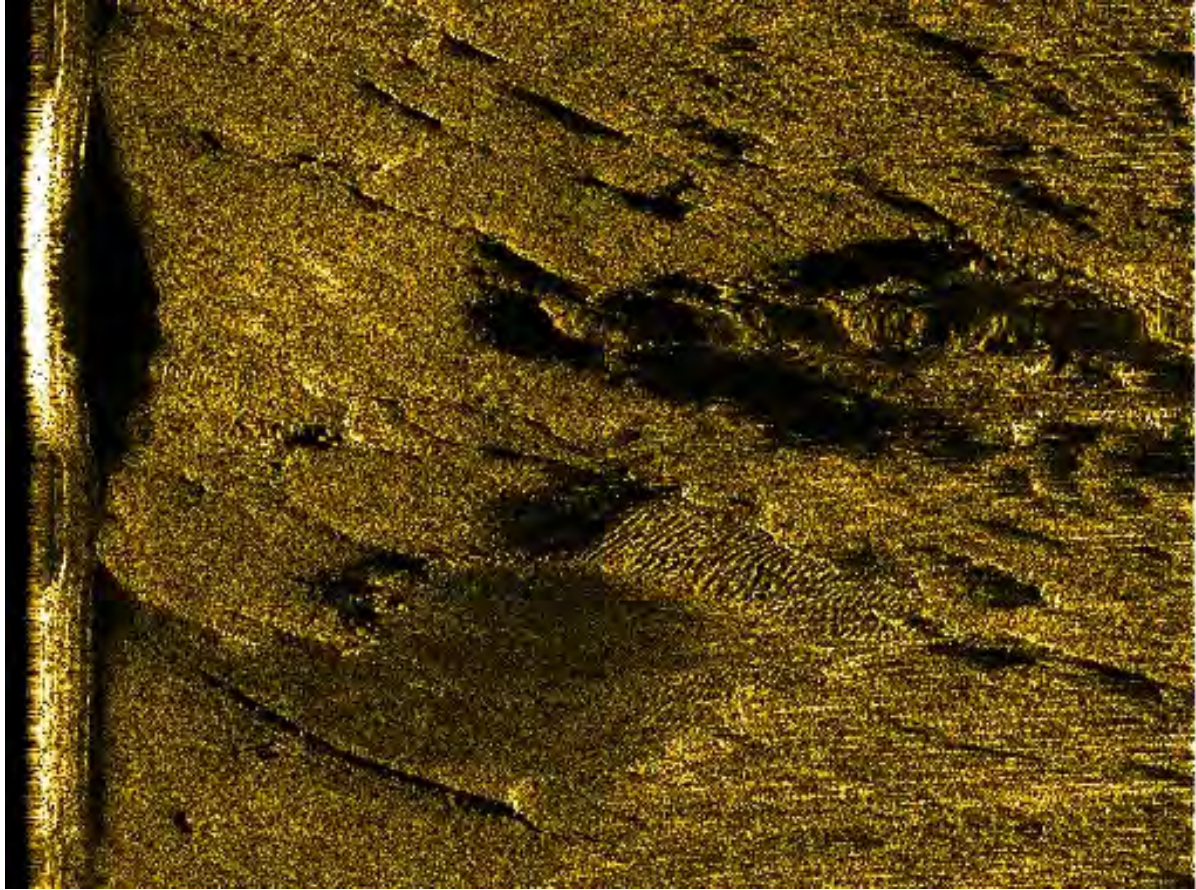
Figure S14. Image showing areas of "ripple" bedform surrounded by microbial bioherms in the south arm of GSL. The occurrence of ripple marks indicates that the area has been affected by wave or current energy sufficient to disturb and remobilize the sediment. Bioherms and sediment are located above wave base.
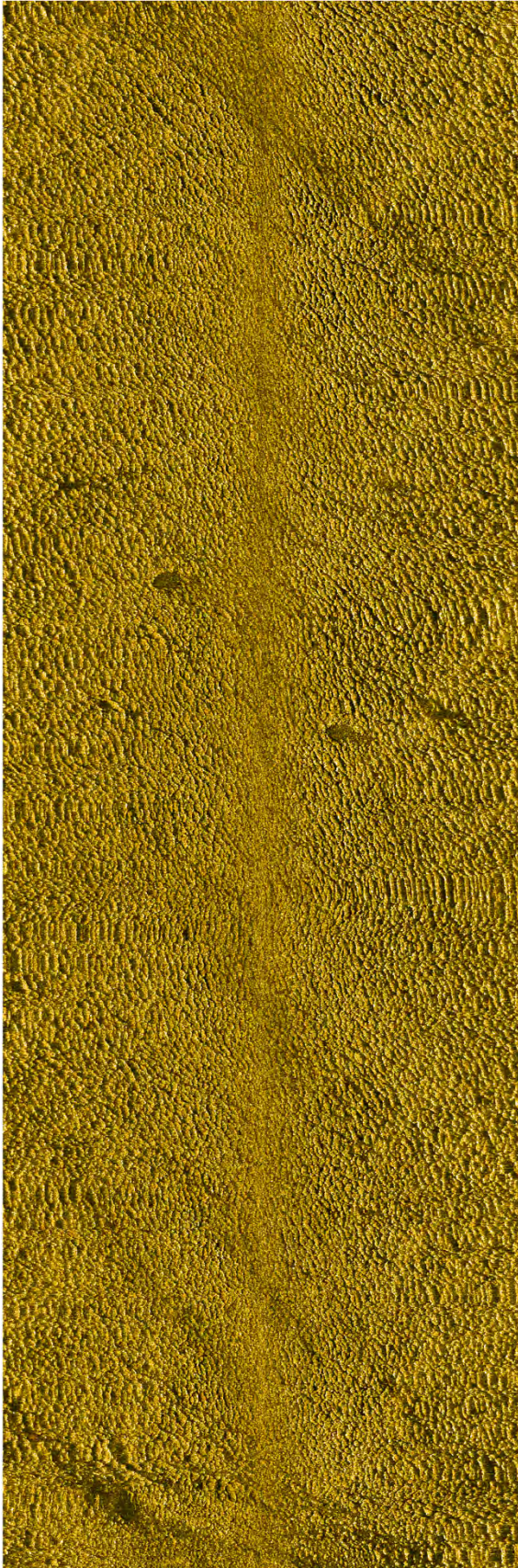
Figure S15. Side scan sonar imagery showing pavement of continuous intergrowth microbial bioherms northeast of Hat Island in GSL. Microbial bioherms occur ca 2.2 m below water surface. Lake surface elevation ca 1,276 m amsl. Image date is 2009 07 09.
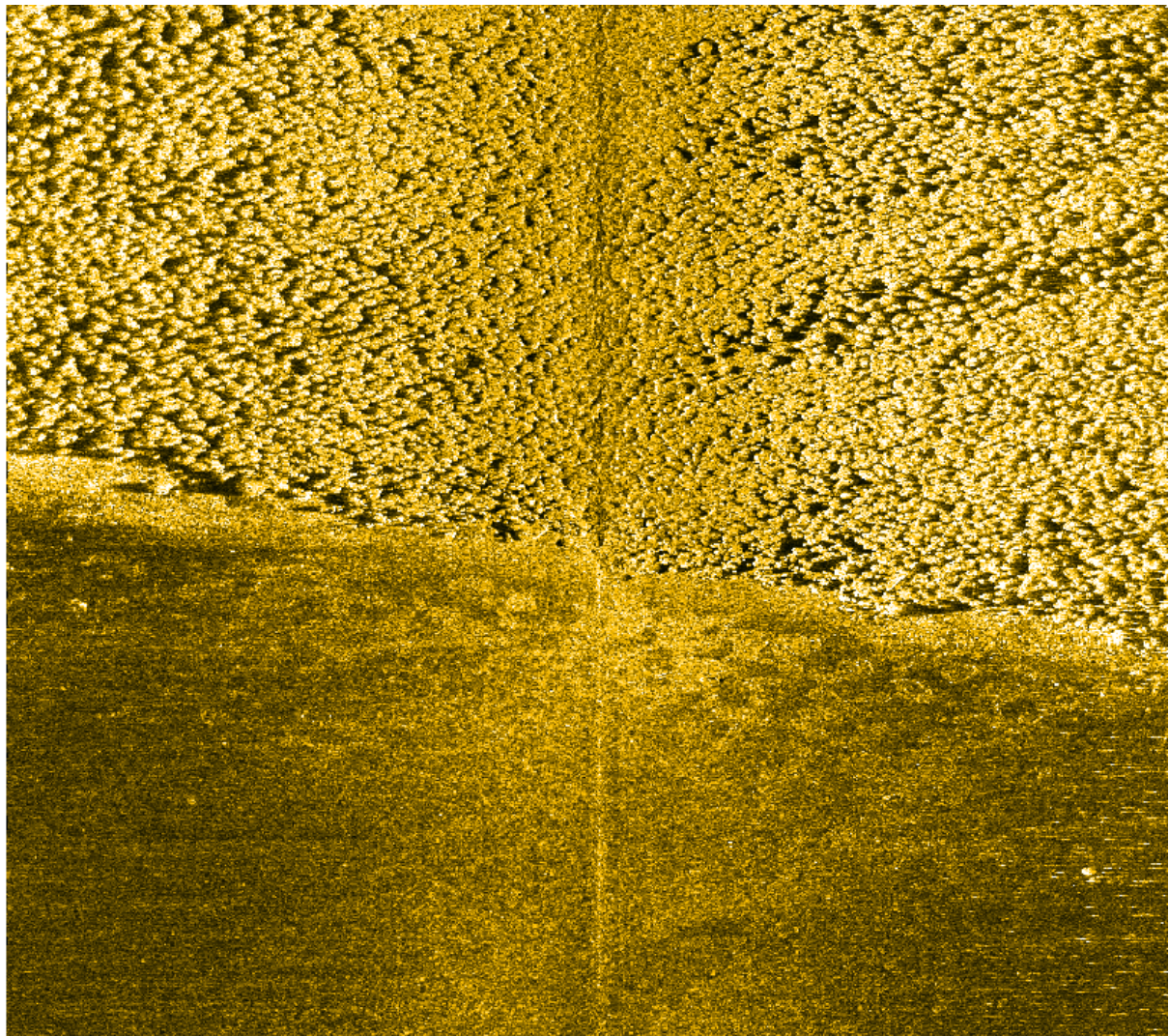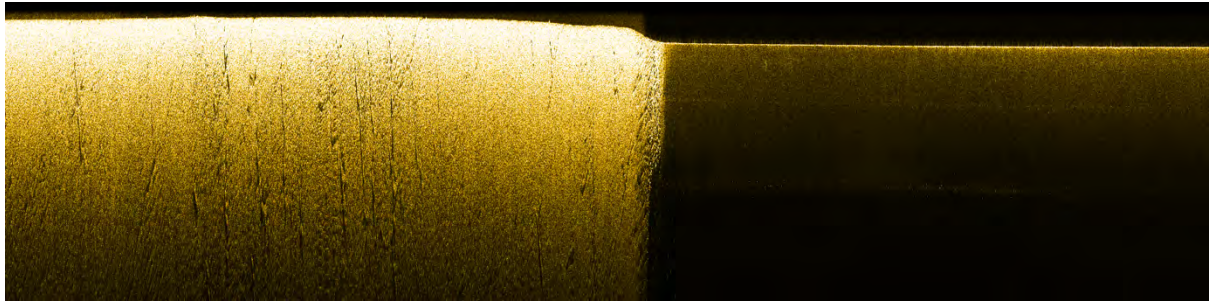
Figure S16. Side scan sonar images showing abrupt transition between continuous intergrowth microbial bioherms and fine-grained sediments along a fault East of Stansbury Island, in the south arm of GSL. At the top, perspective view looking through water column down scan and sidescan along sediment/water interface using port-side beam scans. Offset is 0.5 m. At the bottom, view integrating port and starboard imagery with water column removed. Image date is 2011 03 30. Lake surface elevation 1,278.9 m amsl.

Table S1. Results of stable carbon and oxygen isotope measurements of the Great Salt Lake carbonates (SD = Standard Deviation).

Sample	Fabric	Sample type	$\delta^{13}C$	SD $\delta^{13}C$	$\delta^{18}O$	SD $\delta^{18}O$
BB8-3	Clotted peloidal micrite-grade carbonate	Bridger Bay shoreline exposed bioherm	3.02	0.02	-6.04	0.07
PP3	Clotted peloidal micrite-grade carbonate	Promontory Point shoreline exposed bioherm	3.64	0.02	-5.01	0.04
PP8-1	Clotted peloidal micrite-grade carbonate	Promontory Point shoreline exposed bioherm	2.82	0.03	-4.73	0.03
PP1-4	Clotted peloidal micrite-grade carbonate and internal sediment	Promontory Point shoreline exposed bioherm	3.60	0.03	-5.20	0.04
PP1-2	Clotted peloidal micrite-grade carbonate	Promontory Point shoreline exposed bioherm	3.78	0.03	-5.36	0.03
PO2	Clotted peloidal micrite-grade carbonate and internal sediment	Sublittoral Promontory Point bioherm	3.29	0.02	-5.05	0.03
BB8-4	Spherulitic fabric	Bridger Bay shoreline exposed bioherm	5.62	0.02	-5.19	0.10
BB4	Spherulitic fabric and internal sediment	Bridger Bay shoreline exposed bioherm	4.75	0.02	-5.33	0.03
BB8-1	Spherulitic fabric and internal sediment	Bridger Bay shoreline exposed bioherm	4.86	0.02	-4.68	0.07
BB8-1	Spherulitic fabric and internal sediment	Bridger Bay shoreline exposed bioherm	4.33	0.02	-4.61	0.08
BB8-2	Spherulitic fabric	Bridger Bay shoreline exposed bioherm	4.36	0.01	-4.50	0.07
BO3	Spherulitic fabric	Sublittoral Bridger Bay bioherm	4.48	0.02	-4.76	0.12
PP1-3	Spherulitic fabric	Promontory Point shoreline exposed bioherm	5.17	0.02	-5.16	0.04
PP4	Spherulitic fabric	Promontory Point shoreline exposed bioherm	4.36	0.02	-4.64	0.05
PP2-1	Spherulitic fabric	Promontory Point shoreline exposed bioherm	5.12	0.03	-5.25	0.02
PO1	Spherulitic fabric	Sublittoral Promontory Point bioherm	4.63	0.02	-5.36	0.02
PP2-2	Laminated micrite-grade carbonate	Promontory Point shoreline exposed bioherm	3.08	0.02	-5.39	0.02
PP8-2	Laminated micrite-grade carbonate	Promontory Point shoreline exposed bioherm	4.21	0.02	-5.65	0.03
PP1-1	Laminated micrite-grade carbonate	Promontory Point shoreline exposed bioherm	4.06	0.02	-5.82	0.05
	Average bioherms		**4.17**	**0.79**	**-5.14**	**0.42**
BB2	Ooids	Bridger Bay	4.08	0.01	-4.79	0.03
BB6	Ooids	Bridger Bay	3.84	0.01	-5.28	0.05
	Average ooids		**3.96**	**0.17**	**-5.04**	**0.35**
PB1-1	Clotted peloidal micrite-grade carbonate	Promontory Point coatings on substrate rock boulders	2.57	0.02	-5.22	0.03
PB1-2	Clotted peloidal micrite-grade carbonate	Promontory Point coatings on substrate rock boulders	1.21	0.04	-3.97	0.06
PB3	Clotted peloidal micrite-grade carbonate, internal sediment and fibrous cement	Promontory Point coatings on substrate rock boulders	5.11	0.03	-3.39	0.04
PB3-1	Clotted peloidal micrite-grade carbonate, internal sediment and fibrous cement	Promontory Point coatings on substrate rock boulders	4.87	0.04	-3.45	0.05
	Average coatings		**3.44**	**1.88**	**-4.01**	**0.85**

Great Salt Lake carbon and oxygen stable isotope geochemistry of microbial bioherms and associated sediment

Stable oxygen and carbon isotope samples were microdrilled to separate different fabric types. Twenty-five O and C isotope analyses were performed using a MAT253 mass spectrometer with automated carbonate preparation device (Gas bench II) at the Institute for Geology, Mineralogy and Geophysics stable isotope facility, University of Bochum, Germany. Stable isotope results were calibrated to the VPDB scale by the international standards CO-1 and CO-8. The analytical precision was better than 0.07 ‰ for $\delta^{13}C$ and 0.13 ‰ for $\delta^{18}O$.

Bioherm carbonate stable isotope analyses (19 samples; Figure S17; Table S1) yield average $\delta^{13}C$ 4.2 ‰ (standard deviation SD 0.8 ‰) and average $\delta^{18}O$ -5.1 ‰ (SD 0.4 ‰). The stable isotope signatures of the various fabrics in shoreline exposed and sublittoral bioherms do not show significant differences, even though spherulitic boundstone textures show slightly higher $\delta^{13}C$ values (between 4.4 and 5.6 ‰). Samples that include some trapped internal sediment of peloids and ooids have slightly lower $\delta^{13}C$ values. Ooids (2 samples) show similar $\delta^{18}O$ values -5.0 ‰ (SD 0.4 ‰) and slightly lower $\delta^{13}C$ 4.0 ‰ (SD 0.2 ‰).

Older carbonate coatings on beach boulders from Promontory Points (4 samples) consist of the same carbonate fabrics as the shoreline and sublittoral bioherms and show slightly higher $\delta^{18}O$ values of -4.0 ‰ (SD 0.9 ‰) and lower variable $\delta^{13}C$ values with average 3.4 ‰, but standard deviation of 1.9 ‰.

Stable carbon and oxygen isotope interpretation

Stable C and O isotopes of lacustrine carbonates reflect the isotopic composition of lake water and dissolved inorganic carbon. As summarised in Della Porta (2015), positive correlations of high O and C isotope values indicate closed lakes with long residence time, high evaporation and equilibration of the DIC with atmospheric carbon dioxide (Talbot, 1990, Leng and Marshall, 2004; Hoefs, 2009). The older carbonate coatings on boulders at Promontory Point with the same fabric as sub-littoral microbial bioherms but evidence of meteoric dissolution and neomorphism suggest that meteoric diagenesis might have affected their $\delta^{18}O$ towards higher values and lowered the $\delta^{13}C$ to 1 ‰.

The stable isotope signature recognized in the GSL microbial bioherms and ooids reported in Della Porta (2015) and in this study is similar to the data relative to the ooids published by Pedone and Norgauer (2002) with values of $\delta^{18}O$ -5 ‰ and $\delta^{13}C$ 3.9 ‰ VPDB. The ooid oxygen isotope values are in agreement with carbonates precipitating at equilibrium with water with $\delta^{18}O$ = -5.2 ‰ (SMOW) (Pedone and Norgauer, 2000). Newell et al. (2017) obtained similar values for GSL carbonates and showed that most of the measured $\delta^{18}O$ values are in equilibrium with modern lake water $\delta^{18}O$ ranging approximately between -1 and -4 ‰ (SMOW).

Newell et al. (2017) confirmed that water exchange with atmospheric CO_2 is a major contributor to near-surface DIC in GSL. Newell et al. (2017) also demonstrated from the O, C and N isotope data that although GSL has been a saline lake since 13 ka, it has experienced periods of relatively lower salinity that differed significantly from periods of high salinity and stable meromixis, similar to modern GSL. Lake Bonneville carbonates yield positive stable

isotope correlations consistent with a closed basin with wetter and cooler conditions than the GSL record (Newell et al., 2017).

The spread of $\delta^{13}C$ values of the microbial bioherm clotted peloidal micrite and spherulitic fabrics from ca. +3 to +6 ‰ might suggest the influence of some microbially mediated processes such as photosynthesis, sulphate reduction or microbial respiration (Londry and Des Marais, 2003; Andres et al., 2006; Heindel et al., 2010). Many recent and ancient microbialites do not show evidence of carbon isotope fractionation related to microbially mediated process (Reitner et al., 1995; Della Porta, 2015 and references therein). Nevertheless, Ingalls et al. (2020) proposed for GSL carbonates that some values might reflect local isotopic disequilibrium driven by microbial metabolism during authigenic carbonate precipitation.
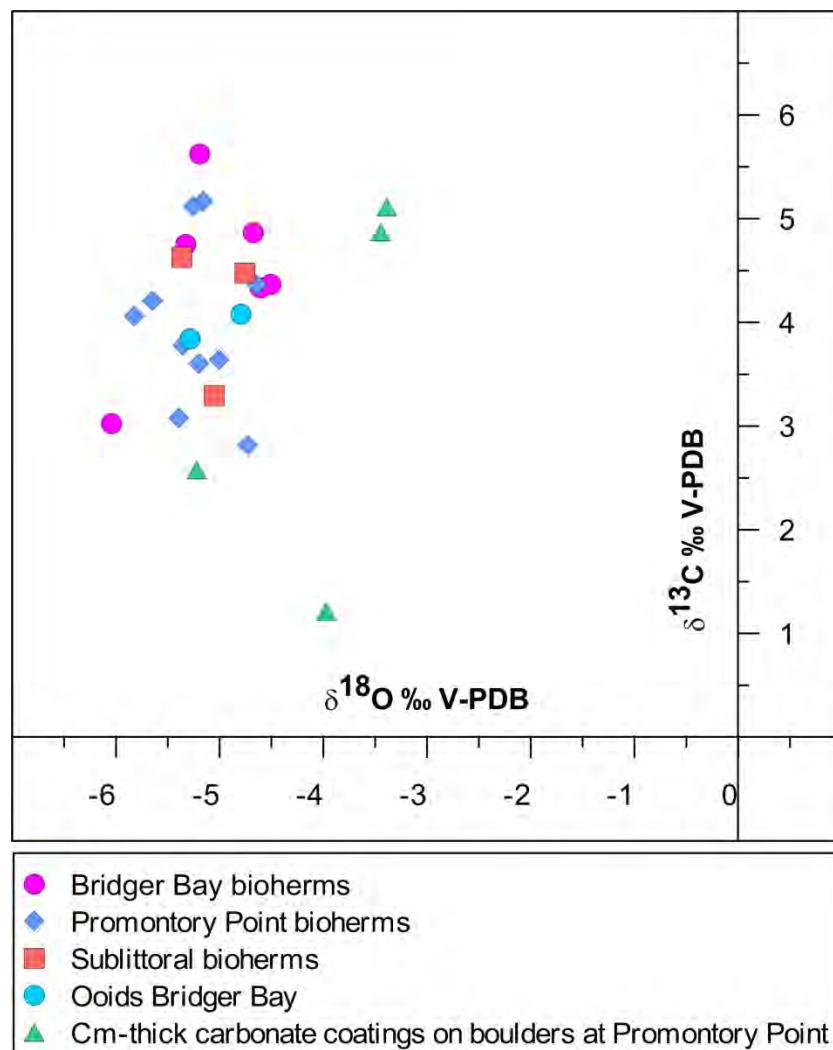

Figure S17. Diagram plotting the results of the stable oxygen and carbon isotope measurements of GSL bioherms and ooids. Present-day bioherms show relatively uniform $\delta^{18}O$ values comprised between -5 and -6 ‰ and $\delta^{13}C$ values ranging approximately from 3 to 6 ‰. There is not an evident difference between bioherm samples collected at Bridger Bay and Promontory Point shorelines and from sublittoral locations at 3-4 m of depth. Microbial bioherms are compared with stable isotope values from old crusts coating boulders on the Promontory Point shoreline, which show resetting of isotopic signature, possibly by meteoric fluids. Data from analysed samples in this study confirm results from Pedone and Norgauer (2000), Newell et al. (2017) and Ingalls et al. (2020).

References

Andres, M.S., Sumner, D.Y., Reid, R.P. and Swart, P.K. (2006) Isotopic fingerprints of microbial respiration in aragonite for Bahamian stromatolites. *Geology*, 34, 973-976.

Della Porta, G. (2015) Carbonate build-ups in lacustrine, hydrothermal and fluvial settings: comparing depositional geometry, fabric types and geochemical signature, in: Bosence, D.W.J., Gibbons, K.A., Le Heron, D.P., Morgan, W.A., Pritchard, T., Vining, B.A. (Eds.), Microbial Carbonates in Space and Time: Implications for Global Exploration and Production. Geol. Soc. London Spec. Publ. 418, 17-68.

Heindel, K., Birgel, D., Peckmann, J., Kuhnert, H. Westphal, H. (2010) Formation of deglacial microbialites in coral reefs off Tahiti (IODP 310) involving sulphate-reducing bacteria. *Palaios*, 25, 618-635.

Hoefs, J. (2009) Stable Isotope Geochemistry. 6th ed. Springer, Berlin.

Ingalls, M., Frantz, C.M., Snell, K.E. and Trower, E.J. (2020) Carbonate facies-specific stable isotope data record climate, hydrology, and microbial communities in Great Salt Lake, UT. *Geobiology*, 18(5), 566-593.

Leng, M.J. and Marshall, J.D. (2004) Palaeoclimate interpretation of stable isotope data from lake sediment archives. *Quaternary Science Reviews,* 23, 811-831.

Londry, K.L. and Des Marais, D.J. (2003) Stable carbon isotope fractionation by sulphate reducing bacteria. *Applied and Environmental Microbiology*, 69, 2942–2949.

Newell, D.L., Jensen, J.L., Frantz, C.M. and Vanden Berg, M.D. (2017) Great Salt Lake (Utah) microbialite $\delta^{13}C$, $\delta^{18}O$, and $\delta^{15}N$ record fluctuations in lake biogeochemistry since the late Pleistocene. *Geochemistry, Geophysics, Geosystems*, 18, 3631-3645.

Pedone, V.A. and Norgauer, C.H. (2002) Petrology and geochemistry of recent ooids from the Great Salt Lake, Utah. In Gwynn, W. (ed.), Great Salt Lake - An overview of change: Special publication of the Utah Department of Natural Resources, Utah Geological Survey, 33–41.

Reitner, J., Neuweiler, F., Gautret, P. (1995) Modern and fossil automicrites: implications for mud mound genesis. In: Reitner, J. and Neuweiler, F. (coord.) A Polygenetic Spectrum of Fine-Grained Carbonate Buildups. Facies, 32, 4–17.

Talbot, M.R. (1990) A review of the palaeohydrological interpretation of carbon and oxygen isotopic ratios in primary lacustrine carbonates*. Chemical Geology: Isotope Geoscience Section*, 80.4, 261–279.